12-2021

Nonmetallic Jet Impingement Thermal Management for Power Electronics via Additive Manufacturing

Reece Whitt
University of Arkansas, Fayetteville

Nonmetallic Jet Impingement Thermal Management for Power Electronics via Additive Manufacturing

A thesis submitted in partial fulfillment
of the requirements for the degree of
Master of Science in Mechanical Engineering

by

Reece Whitt
University of Arkansas
Bachelor of Science in Mechanical Engineering, 2018

December 2021
University of Arkansas

David Huitink, Ph.D.
Thesis Director

Han Hu, Ph.D.
Committee Member

Yue Zhao, Ph.D.
Committee Member

ABSTRACT

The increase in energy demanded by transportation and energy sectors has necessitated highly efficient thermal management for reliable power electronics operations. Conventional cooling techniques are limited by their inability to target switching location hot spot temperatures, leading to non-uniform thermal gradients. These devices, such as cold plates and heat sinks, also utilize heavy metallic structures that can accentuate electromagnetic interferences generated by high voltage switching processes. This work proposes a non-metallic jet impingement cooler for more customized thermal management, while simultaneously reducing the harmful effects of electromagnetic interferences. Additive manufacturing is utilized to enable jet impingement zones to target individual power module hot spots in a lightweight, electrically isolating framework. Simulated and experimental results with die-mimicking capabilities show the ability of reducing maximum junction temperatures by 30 °C and eliminating cross-module temperature gradients by 90%. Integrated testing with a 150kW silicon carbide MOSFET based inverter show a 25dB drop in common mode noise as a result of a 99% reduction in parasitic capacitance pathways through the thermal management system. Furthermore, multiple jet impingement devices integrated with a single-phase inverter setup is demonstrated as a method to thermally balance electrical devices through hydraulic circuit networks.

ACKNOWLEDGEMENTS

Many thanks to my advisor, Dr. David Huitink, for his guidance and mentorship during my time as both an undergraduate and master's research assistant. His daily expert advice, countless hours of project management and willingness to go the extra mile will always be held very highly. Thank you also to my advisory committee for their guidance during the process of completing these degree requirements.

To my fellow EMPIRE laboratory colleagues, your help with course work, experimental setups and many other activities is a big reason why this research can exist. My time working with each of you will always be cherished.

I would also like to thank the University of Arkansas Mechanical Engineering department for their assistance and incredibly rewarding coursework to enable graduate students to directly apply topics to their research. Special thanks to Jason Bailey, Monty Roberts, and Ben Fleming for their experimental hardware assistance.

Lastly, I want to thank my family. Thank you, Mom, Dad and Remington, for your loving support throughout this process. To my extended family, I am very appreciative for all the generosity and words of reassurance you have provided. And to my wife, Ember, thank you for taking this journey with me. Your love and encouragement provided a stable rock to stand on.

DEDICATION

To my family for their strong support system that made this possible

To my wife Ember for her words of encouragement and patient understanding

TABLE OF CONTENTS

LIST OF PUBLISHED PAPERS

Chapter 3:

R. Whitt, D. Huitink, A. Emon, A. Deshpande, and F. Luo, "Thermal and Electrical Performance in High-Voltage Power Modules With Nonmetallic Additively Manufactured Impingement Coolers," IEEE Transactions on Power Electronics, vol. 36, no. 3, pp. 3192-3199, 2021, doi: 10.1109/TPEL.2020.3015226.

Chapter 4:

R. Whitt, S. J. Hudson, D. Huitink, Z. Yuan, A. Emon, and F. Luo, "Additive Manufactured Impinging Coolant, Low EMI, & Non-Metallic Heat Spreader: Design and Optimization," Journal of Electronic Packaging.

1. CURRENT POWER ELECTRONICS CHALLENGES

1.1 POWER ELECTRONICS TRENDS

The current trend of automotive and aerospace transportation is the push for hybrid and full electric propulsion. Driven primarily by the need to remove non-renewable resources from the energy supply chain when feasible, on-board battery power and generators provide most of the useful energy for electric motors [1]. The conversion process between battery power and kinetic energy of the system occurs at the heart of the power electronic system. For electric vehicles, high frequency switching processes convert stored DC current into AC current for motors and other peripheral electrical components [2]. As the demand for more efficient electric machines grows [3], the conversion equipment must continue to increase the total power density and specific power for the take of total efficiency improvement. Regarding electric vehicles and hybrid-electric propulsion systems, the current targets for 2025 set by the DOE are power density ratings over 30 kW/L and a specific power of 20 kW/kg [4]. Given these goals, a design focus of power electronic systems over the past ten years has been to package the internal components in layers, as opposed to a singular plane [5]. Since these power components typically have integrated base plates for cooling purposes, the switching devices towards the middle of the stack can experience higher temperatures due to increased thermal resistances [6]. For example, a specific power electronics inverter architecture known to have high control performance and low noise levels for high switching frequencies is the T-type converter [7]. In this arrangement three levels of components may be present, including power modules, gate drives and capacitors.

No matter the specific architecture chosen, power electronic devices can present intense switching losses in the form of thermal energy that must be removed. Advanced packaging techniques aimed to improve reliability and increase thermal conductivity are being integrated to

achieve more efficient cooling. Base plate materials like aluminum silicon carbide and laminated busbar devices are a few examples where the mismatch of thermal expansion coefficients is reduced, and electronic interferences are dampened [8]. Additionally, double-sided cooling configurations enable two pathways for heat removal, effectively halving the thermal resistance assuming equal construction in reference to the mid-plane [9].

In conjunction with advanced packaging technologies, the system metrics targets set for 2025 rely heavily on the introduction of wide band gap semiconductors to replace standard silicon transistors. Capable of handling temperatures up to 175 °C, high breakdown voltage and switching frequencies in the kHz range, silicon carbide (SiC) and gallium nitride (GaN) materials have been researched extensively and introduced into commercial power modules [10]. The main barriers preventing mass adoption of such materials are cost and manufacturing supply. With wide industry adoption though, the upfront costs are expected to drop [11].

Finally, the connection between the semiconductor device and underlying layers has generally been reliant on wire bonding and soldering processes. As power density increases, these interconnects are especially susceptible to failure driven by temperature fluctuations and CTE mismatch. Newer devices are now using sintering methods for improved thermal conductivity and lower internal stresses at extreme operating conditions [12]. Using pressure, the sintering process creates an interconnect that can finish with a zero-strain temperature around 250 °C but has a melting temperature of 960 °C [13]. Compared to a solder process, the sintered interconnect shows improved fatigue strength and lower accumulated damage.

1.2 LIMITATIONS OF TRADITIONAL THERMAL MANAGEMENT SYSTEMS

Even with the introduction of improved packaging techniques and wide band gap devices, the high switching frequencies demanded by modern electric transportation demands efficient

thermal management. Total heat fluxes ranging from 500 – 1000 kW/cm^2 must be controlled via advanced cooling methods to avoid premature device failure. Without sufficient heat transfer, the electronics may experience a thermal runaway event leading to device failure. Advanced semiconductor materials and interconnects commonly require junction temperatures lower than 175 °C. For this reason, traditional cooling techniques are quickly being replaced. Historically, simple copper-tube cold plates and air-cooled heat sinks have been widely utilized for their easy of manufacturability and system integration [14].

Cold plates use high thermal conductivity metals in contact with electrical systems to transfer thermal energy into convectively cooled internal channels. Thus, a series thermal resistance network exists with major thermal bottlenecks present at the cold plate-electronics interface and the convective efficiency of the internal coolant. Standard off-the-shelf options will usually consist of an aluminum body with passes of copper tubing. As the coolant passes through the tubing, it will extract thermal energy from the power electronics and experience an increase in internal energy. This process will continue until the fluid exits the plate warmer than when it entered. Thermal gradients across the body of the cold plate will be generated simply due to the nonuniform cooling resulting from coolant heating. Figure 1a shows a graphical depiction of how electrical devices might exhibit thermal gradients created by a non-optimized cold plate. Similarly, air cooled heat sinks can also influence the formation of temperature variations [15]. The co-heating of die locations is driven by the reliance on bulk conduction through the body of the heat sink. In the presence of uniform air flow throughout the fins, this effect is accentuated.

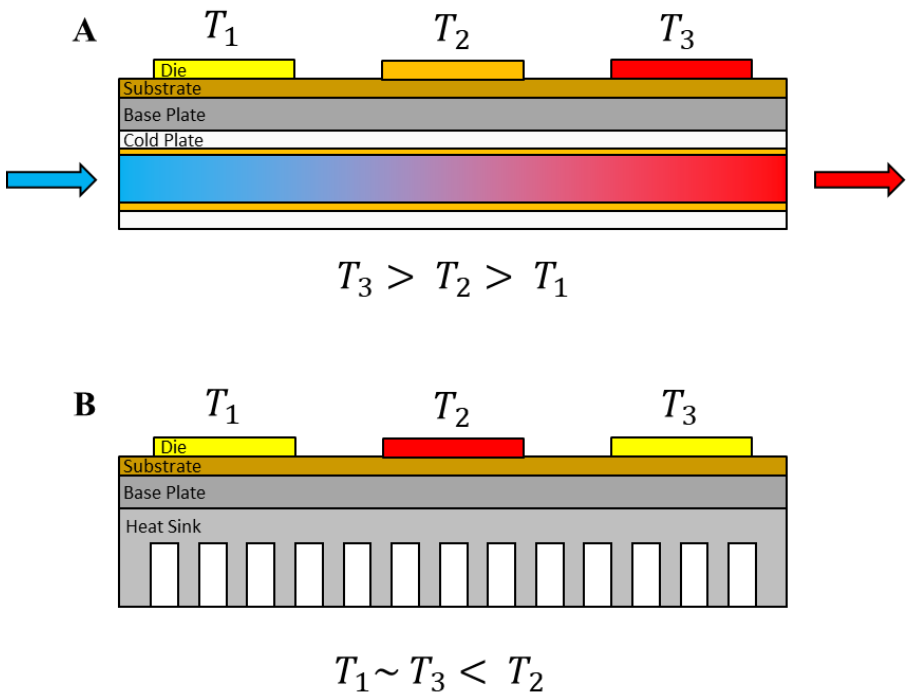

Figure 1: Pictorial depiction of nonuniform die temperatures with a) cold plate and b) heat sink thermal management solutions.

In addition to the limitations involving thermal gradients, cooling solutions which require thermal interface layers and heat removal through bulk conduction have reduced ability to effectively manage hot spots. Consequently, the current sharing between transistor locations can become imbalanced due to variations in on-state resistances [16]. Thermally imbalanced devices operating in parallel, commonly used for more power dense systems, from a physics of failure perspective have varying lifetime predictions. The challenge of overall module reliability then becomes a greater issue.

Finally, thermal management solutions that rely on large-volume metallic components directly integrated with high switching frequency power modules can heighten electromagnetic noise concerns. Stray inductance generated by close-proximity semiconductor devices can affect peripheral components critical for driver circuits. Parasitic capacitance generated by highly conductive materials offer pathways for common mode noise to travel [17]. Thus, the metallic

thermal management parts can contribute towards harmful harmonic emissions and increased switching losses. As required by EMC standards, EMI filters must be present to limit the noise from power electronics operation to the rest of the transportation system. Depending on the severity of the noise levels, up to 30% of system volume and weight can be comprised of filtering components [18]. Therefore, it is reasonable to conclude that non-metallic thermal management parts would aid in reducing filter requirements assuming common mode noise levels are reduced.

Although many publications have focused on improving power electronics thermal management systems, there is a considerable lack of studies integrating non-metallic materials into these high-voltage systems. Whether constrained by manufacturing techniques or cooling capability, common cooling techniques can worsen module reliability through insufficient hot spot management and reduce power density values by requiring additional EMI filtering.

1.3 THESIS OVERVIEW

This work aims to demonstrate the effectiveness of a nonmetallic-based thermal management approach to improve the efficiency of power electronics systems. Using additive manufacturing to construct an advanced liquid jet impingement cooling solution, power density and specific power metrics of a high-voltage hybrid-electric propulsion inverter are increased while simultaneously improving measured EMI levels. Die-level thermal management and integrated inverter testing give insight into the cooling improvements on the module and systematic scales.

Chapter 2 discusses advanced cooling techniques with a focus on high heat flux capable methods. A quick background on fundamental jet impingement physics is provided, in addition to examples of integrated jet impingement coolers.

Chapter 3, the first of two published works, first introduces the proposed impingement cooling method. Computational and experimental performance evaluations are given with comparison to state-of-the art examples. The focus of these activities was to evaluate the average cooling enhancement seen in a T-type power module arrangement. Single-module scale EMI tests are also carried out and discussed in terms of overall noise reduction.

Chapter 4, the second published article, investigates the cooling benefits of the non-metallic cooler in terms of module-scale thermal gradients. Further EMI evaluations are performed.

Chapter 5 details efforts to directly integrate the nonmetallic cooler with a high-voltage inverter system. The thermal balancing of multiple power modules using hydraulic circuits is demonstrated, with an analysis into when each configuration is applicable.

Finally, in terms of design requirements, Table 1 details an overview of functional objectives for the design, manufacturing, and integration of the cooler. The underlying physical mechanisms guiding geometry selections such as nozzle size and overall cooler height are outlined in Chapter 2. The manufacturing methods are largely dictated by factors including 3D printing cost and process availability. And the integration techniques, as further described in Chapter 5, are directly associated with the assembly of the SiC power module used in the high-voltage inverter.

TABLE 1

Objective Area	Design	Manufacturing	Integration
Requirements	$2 < H/D < 8$	Nonmetallic materials	Four through-hole mounting locations matching inverter power modules
	$10{,}000 < Re < 50{,}000$	Additive methods	Interface between cooler and module created via gasket. Sealing achieved by mounting pressure
	One nozzle per hot spot	Material heat deflection temperature > 150 °C	Footprint of cooler matches module base plate
	Water used as coolant	Watertight surface. Can be achieved by post processing	One inlet and one outlet coolant path

1.4 REFERENCES

[1] A. Emadi, Y. J. Lee, and K. Rajashekara, "Power Electronics and Motor Drives in Electric, Hybrid Electric, and Plug-In Hybrid Electric Vehicles," IEEE Transactions on Industrial Electronics, vol. 55, no. 6, pp. 2237-2245, 2008, doi: 10.1109/TIE.2008.922768.

[2] X. Xu and V. A. Sankaran, "Power electronics in electric vehicles: challenges and opportunities," Conference Record of the 1993 IEEE Industry Applications Conference Twenty-Eighth IAS Annual Meeting, 1993, pp. 463-469 vol.1, doi: 10.1109/IAS.1993.298964.

[3] Zhou, Y., Wang, M., Hao, H. et al. Plug-in electric vehicle market penetration and incentives: a global review. Mitig Adapt Strateg Glob Change 20, 777–795 (2015). https://doi.org/10.1007/s11027-014-9611-2

[4] S. Chowdhury, E. Gurpinar, G. -J. Su, T. Raminosoa, T. A. Burress and B. Ozpineci, "Enabling Technologies for Compact Integrated Electric Drives for Automotive Traction Applications,"

2019 IEEE Transportation Electrification Conference and Expo (ITEC), 2019, pp. 1-8, doi: 10.1109/ITEC.2019.8790594.

[5] C. Chen, F. Luo and Y. Kang, "A review of SiC power module packaging: Layout, material system and integration," in CPSS Transactions on Power Electronics and Applications, vol. 2, no. 3, pp. 170-186, Sept. 2017, doi: 10.24295/CPSSTPEA.2017.00017.

[6] G. Ghaisas and S. Krishnan, "A Critical Review and Perspective on Thermal Management of Power Electronics Modules for Inverters and Converters," Transactions of the Indian National Academy of Engineering, 2021/09/24 2021, doi: 10.1007/s41403-021-00268-1.

[7] M. Schweizer and J. W. Kolar, "Design and Implementation of a Highly Efficient Three-Level T-Type Converter for Low-Voltage Applications," in IEEE Transactions on Power Electronics, vol. 28, no. 2, pp. 899-907, Feb. 2013, doi: 10.1109/TPEL.2012.2203151.

[8] Z. Yuan et al., "Design and Evaluation of Laminated Busbar for Three-Level T-Type NPC Power Electronics Building Block With Enhanced Dynamic Current Sharing," in IEEE Journal of Emerging and Selected Topics in Power Electronics, vol. 8, no. 1, pp. 395-406, March 2020, doi: 10.1109/JESTPE.2019.2947488.

[9] G. Moreno, S. Narumanchi, X. Feng, P. Anschel, S. Myers, and P. Keller, "Electric-Drive Vehicle Power Electronics Thermal Management: Current Status, Challenges, and Future Directions," Journal of Electronic Packaging, vol. 144, no. 1, 2021, doi: 10.1115/1.4049815.

[10] J. Reimers, L. Dorn-Gomba, C. Mak and A. Emadi, "Automotive Traction Inverters: Current Status and Future Trends," in IEEE Transactions on Vehicular Technology, vol. 68, no. 4, pp. 3337-3350, April 2019, doi: 10.1109/TVT.2019.2897899.

[11] S. Das, L. D. Marlino, and K. O. Armstrong, “Wide bandgap semiconductor opportunities in power electronics,” Oak Ridge National Lab., Oak Ridge, TN, USA, Tech. Rep. ORNL/TM-2017/702, 2018.

[12] Y. Zhao et al., "Silver sintering die attach process for IGBT power module production," 2017 IEEE Applied Power Electronics Conference and Exposition (APEC), 2017, pp. 3091-3094, doi: 10.1109/APEC.2017.7931138.

[13] M. Calabretta, A. Sitta, S. M. Oliveri, and G. Sequenzia, "Silver Sintering for Silicon Carbide Die Attach: Process Optimization and Structural Modeling," Applied Sciences, vol. 11, no. 15, 2021, doi: 10.3390/app11157012.

[14] G. Moreno, K. Bennion, C. King and S. Narumanchi, "Evaluation of performance and opportunities for improvements in automotive power electronics systems," 2016 15th IEEE Intersociety Conference on Thermal and Thermomechanical Phenomena in Electronic Systems (ITherm), 2016, pp. 185-192, doi: 10.1109/ITHERM.2016.7517548.

[15] A. G. Fedorov and R. Viskanta, "Three-dimensional conjugate heat transfer in the microchannel heat sink for electronic packaging," International Journal of Heat and Mass

Transfer, vol. 43, no. 3, pp. 399-415, 2000/02/01/ 2000, doi: https://doi.org/10.1016/S0017-9310(99)00151-9.

[16] X. Wang, Z. Zhao and L. Yuan, "Current sharing of IGBT modules in parallel with thermal imbalance," 2010 IEEE Energy Conversion Congress and Exposition, 2010, pp. 2101-2108, doi: 10.1109/ECCE.2010.5618253.

[17] F. Zare, D. Kumar, M. Lungeanu and A. Andreas, "Electromagnetic interference issues of power, electronics systems with wide band gap, semiconductor devices," 2015 IEEE Energy Conversion Congress and Exposition (ECCE), 2015, pp. 5946-5951, doi: 10.1109/ECCE.2015.7310494.

[18] F. Luo, B. Narayanasamy And A. Emon, "High Power Density Emi Mitigation In Power Electronics Converters: Active And Integrated Solutions," Cips 2020; 11th International Conference On Integrated Power Electronics Systems, 2020, Pp. 1-6.

2. THERMAL MANAGEMENT FOR POWER ELECTRONICS

2.1 ADVANCED THERMAL MANAGEMENT APPROACHES

Thermal losses in power electronics modules are quickly approaching 500 W/cm^2 [1]. Primarily limited by packaging materials and methods, maximum junction temperatures are limited to 175 °C to avoid premature failure modes such as delamination, warpage, wire bond liftoff and solder ball cracking. To achieve these ambitious system parameters for future power electronics systems, the primary goal of advanced thermal management solutions is to reduce the thermal resistance of the electronics using two methods: bringing the cooling medium closer to the switching devices and integrating high heat transfer coefficient cooling approaches. For this purpose of this chapter and relevance to the thesis objectives, the focus will be on the improved cooling methods. To start, figure 2 presents a breakdown of the three main types of thermal management types that have been improved using advanced techniques.

In terms of heat transfer capacity, forced liquid cooling methods, on average, can be two times or more than standard forced air convection [2]. At 25 °C, the specific heat capacities for air and water at constant pressure are 1.006 kJ/(kg*K) and 4.18 kJ/(kg*K), respectively. By default, liquid methods have a clear advantage. Even with air heat sink advancements such as 3D printed micro features [3], fractal shapes designed with genetic algorithms [4] and turbulence generators [5], maximum heat fluxes achieved for air cooling can range between 50-100 W/cm^2 [6]. For this reason, the remaining portions of the chapter will focus on a brief review of three liquid cooling solutions: microchannel, jet impingement and spray cooling.

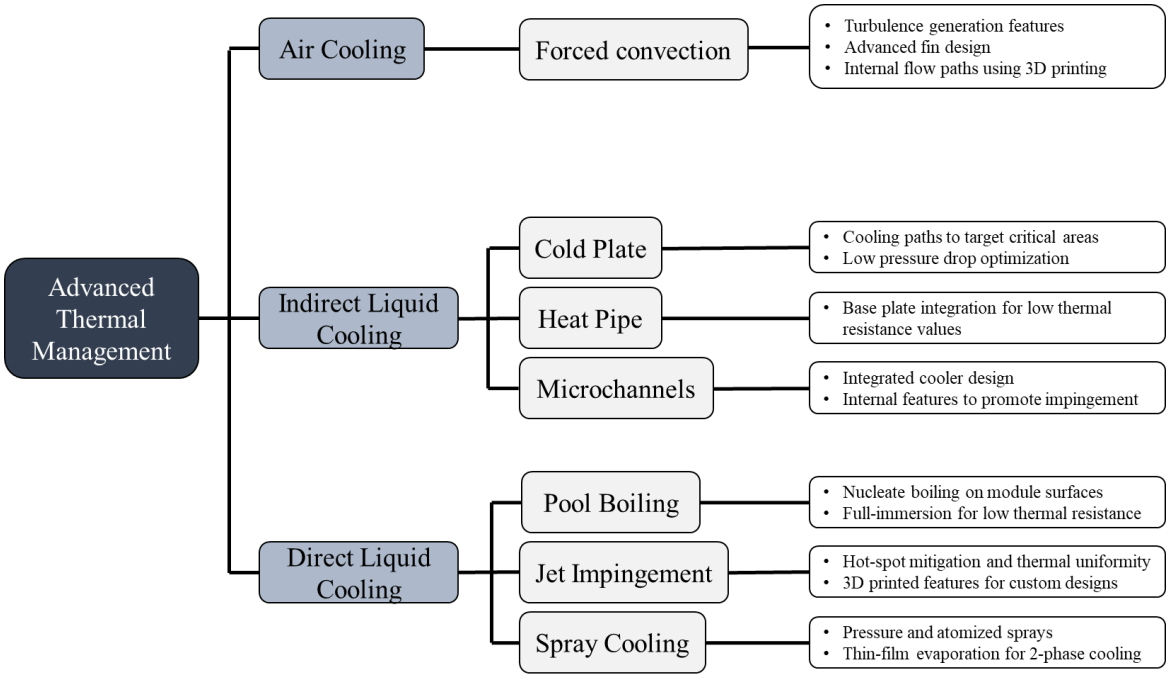

Figure 2: Flow chart of advanced thermal management techniques

2.1.1 MICROCHANNEL

The primary working principle for novel microchannel coolers is to optimize the ratio of heat transfer ability to pumping power [7]. The small internal features, commonly tens to hundreds of microns, generate immense pressure drop that is shown to be proportional to the quadratic of the channel aspect ratio [8], while the Nusselt number is highly dependent on the surface area and equivalent hydraulic diameter of the channels. Methods to subdue pressure drop effects is to minimize the overall channel lengths and only utilize narrow channels near critical hot spots. However, there still exists a sharp relationship between the heat transfer ability and pressure drop given the scale of the cooler features and the increase in module power density. Tuckerman et al. [9] demonstrated a high heat flux water-based cooler with a heat flux of 790 W/cm^2 over a footprint of 10 x 10 mm and 50 µm channels. However, the corresponding pressure drop was well above 300 kPa, which would be difficult to achieve in electrified transportation systems.

One method recently proposed is the integration of microchannels in the substrate of high-voltage devices. Jung et al. achieved a 250 W/cm^2 heat flux with less than 3 kPa of pressure drop [10]. Moreover, their computational fluid simulations showed a theoretical 850 W/cm^2 at the same pressure and flow rate. The microchannel features were embedded using a combination of silicon etching and the deposition of Au-Si layers. In the end, a sealed component was produced with the potential to be directly integrated with advanced semiconductor devices.

Microchannel cooling has great potential for high heat flux removal of power electronics losses. However, the main features preventing mass adoption, as mentioned before, are the associated pressure drops, fabrication costs and risks of clogging. A sealed channel located on a critical hot spot might cause a thermal runaway event. Intense pressure drops may not be compatible with electrical systems. And the meticulous etching and layer deposition process creates large costs.

2.1.2 SPRAY COOLING

Compared to microchannel methods that rely on convection-based heat transfer through solid material, spray cooling leverages a coolant's latent heat of evaporation for thermal management. Impinging sprays can be generated with one of two techniques: pressure-based and atomization. The droplets that are created impinge onto the target surface and depending on specific parameters such as wettability, target temperature and boiling regime, can create enable heat fluxes up to 1200 W/cm^2 [11]. The heat transfer capability of impinging sprays can be broken down into three regimes.

First is spray cooling without phase change. If the target surface does not transfer enough thermal energy to begin the boiling process, the coolant droplets rely primarily on conduction for heat transfer. The impinged droplets quickly form a liquid film on the target wall with low Nusselt

numbers, identifying little heat transfer enhancement due to convection. Predicting the cooling capability of this regime is strongly dependent on simplified physical models to describe the complex and random bubble hydrodynamics [12].

The second regime spray cooling might fall into is nucleate boiling. Impinged droplets quickly change phase because of nucleation sites formed by sufficient target plate thermal energy. If dry out conditions are avoided, this regime offers the highest heat flux for spray cooling technology. During boiling, the droplets will grow proportional to the square root of the time spent on the target wall. The bubble will then lift off once the buoyant forces overcome the liquid surface tension, allowing for more bubbles to form [12]. The maximum heat transfer condition for nucleate boiling is known as the critical heat flux occurs when the bubble dwell time decreases to the point where a vapor column forms and is continuously fed by liquid coolant on the target face.

Lastly, if the impinging spray passes the Leidenfrost point with respect to removed heat flux, a film of vapor will form between the liquid coolant and target wall. Like spray cooling without boiling, the film does not allow for additional coolant to attach to the wall and change phases. Thus, the hot target plate is separated from the coolant by a low conductivity vapor barrier. If not accounted for, devices in this regime will experience a high temperature gradient with the likelihood of electrical burnout [12].

While capable of excellent heat transfer, spray cooling has its limitations. Clogging may occur in the micron-sized spray nozzles. Up to 300 kPa of pressure is needed to create small enough droplets for effective cooling. And finally, the manufacturing tolerances of the nozzles may vary to an extent as to create non-uniform cooling patterns, leading to varying stress loads in electrical components.

2.1.3 JET IMPINGEMENT

Jet impingement cooling has become a popular choice for extreme heat flux electronic systems. This type of cooler can be easily integrated into a direct cooling arrangement with clear optimization paths regarding heat transfer and pressure drop. Single-phase jets exit a nozzle or orifice where they then quickly impinge onto the target surface. The nozzles are typically positioned directly in-line with critical hot spots for maximum effectiveness. Maximum heat flux values reaching upwards of 2000 W/cm^2 were reported by Silverman et al [13]. And pressure drop values for an impingement cooler can reach up to 48 kPa for micron-sized jets [14].

When comparing maximum heat flux values for jet impingement against microchannels and spray cooling, each method can well exceed the 750 W/cm^2 mark that is commonly deemed to be a requirement for future power electronic systems. Thus, the decision on which method to choose hinges on the pumping power of the cooling system to be integrated with. The pumping costs associated with jet impingement devices can show a reduction of up to 75% compared to the other methods, but with similar cooling capabilities [18].

2.2 JET IMPINGEMENT PHYSICS

Continuing from the last section and the brief discussion of jet impingement cooling, this portion of chapter 2 aims to describe the key physics of impingement and how it directly relates to thermal management efficiency. Figure 3 presents key features and flow regions of a single impinging jet. The three regions, free jet, stagnation, and wall jet, each possess unique characteristics that contribute towards a successful cooling method. The free jet is the initial portion of the fluid flow where it is far enough from the target surface to behave like a free submerged jet. Initial velocity profiles are highly dependent on the nozzle geometry, specifically shape and diameter.

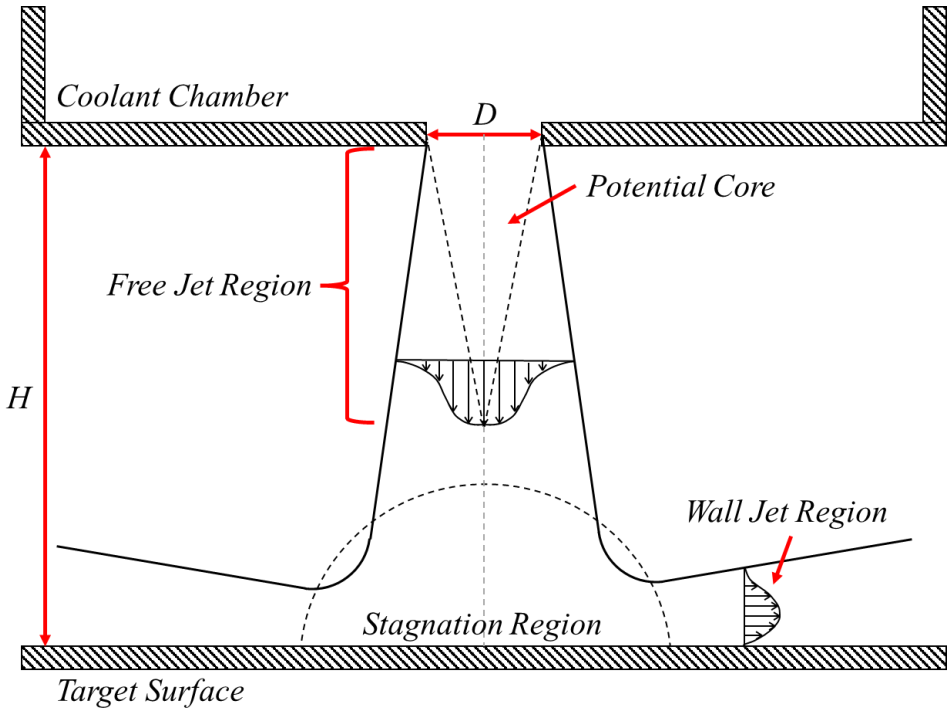

Figure 3: Jet impingement regions and features

Summarized by Zuckerman et al, a pipe nozzle will have a high initial turbulence and high pressure drop, whereas a sharp orifice will have low jet turbulence and high pressure drop [15]. Shearing forces at the edge of the jet causes a lateral momentum shift, entrains external fluid, and begins to flatten the jet velocity profile. Known as turbulent jet expansion, the potential core remains at higher pressure until it converges within 2D of the target surface. From this point, the velocity profile continues to decay, where a fully developed Gaussian curve can be used to represent the mass flow of the jet. Typically, the decaying jet will be present at four to eight nozzle diameters from the nozzle exit [15].

At this point the jet has transferred momentum to surrounding fluid through entrainment and is approaching the target surface. At approximately 1.2 nozzle diameters from the wall, a high-pressure stagnation region forms [15]. The jet decelerates as static pressure increases and begins to turn. In this zone, velocity is minimized leading to a Nusselt number peak typically found at the

center of an axisymmetric jet [15]. Many semi-empirical correlations exist to predict the heat transfer in this zone, and the work by Martin is highly regarded as a key reference for jet impingement fundamentals and fundamental physics [16]. For example, the estimated Nusselt number correlation of a single round jet with a pipe nozzle has been given by Wen et al. [19]. Equation 1 gives the correlation and range of validity regarding the height to diameter ratio, Reynolds number range and the radius from the center line where the equation can be applied. This form is the typical format followed by empirical correlations, as it can be directly related to physical parameters for experimental and analytical analyses. For this specific correlation, integrating the equation over the entire radius range is not necessary to obtain a surface area average as the resulting Nusselt number is the average value.

$$Nu_{avg} = 0.442\, Re^{0.696} Pr^{1/3} (H/D)^{-0.20} (r/D)^{-0.41} \quad (1)$$

$$3 < H/D < 16$$

$$0 < r/D < 7.14$$

$$750 < Re < 27{,}000$$

After the stagnation zone, the fluid enters the wall jet region. First described by Glauert in 1956 [17], the fluid moves outward from the jet center and effectively acts like crossflow over a flat plate. Parameters such as Reynold's number and the ratio of H/D effect the thickness of the thermal boundary layer in the wall jet. For maximum heat transfer, this needs to be minimized and typically occurs 0.75 – 3 nozzle diameters from the jet center [15]. From this point, the wall jet increases in thickness due to the shearing layer between the lateral moving fluid and the velocity of fluid outside this region.

In addition to nondimensional parameters employed to describe the heat transfer of an impinging jet, other key factors that are applicable for integrated cooling systems. First, for a

confined jet, the fluid dynamics is highly responsive to the distance from the nozzle exit to target plate, H. When divided by the hydraulic diameter of the nozzle, D, the H/D ratio can quickly predict overall performance. For an H/D ratio below two, the jet flow is highly constrained by the confinement wall. As a result, the location of the maximum Nusselt number shifts outwards by approximately 1D. Extreme fountain effects created by neighboring jets can affect heat transfer rates and turbulence generation is limited. Therefore, for integration onto a power electronics system, there is a minimum height requirement for an impingement cooler to be effective. For an H/D ratio of two to eight, fluid entrainment occurs between fluid shear layers and the interaction between multiple jets must be considered. In this range, there is sufficient spacing for the jet to fully develop and for a stagnation region to occur, resulting in the best overall performance. Generally, the interaction between jets is not an issue when the distance between nozzles divided by the jet diameter, P/D, is greater than eight. And for an H/D ratio greater than eight, the effect of the confinement wall is minimized. However, the increased spacing quickly decays the kinetic energy of the jet, resulting in reduced Nusselt numbers. In this region, the shape of the nozzle greatly affects performance, as does the interaction between neighboring jets [15].

2.3 CONCLUSION

In general, the elimination of the thermal interface layer using direct cooling approaches has shown immense benefits for hot spot management. While typically having high pressure drops, microchannel and spray cooling techniques have sufficiently high heat flux capacity for modern day power electronics. However, in terms of efficiency with respect to heat transfer rates and corresponding pumping power, jet impingement schemes hold the most potential for the direct cooling of power module base plates. Physical parameters such as the height of the jet and nozzle hydraulic diameter strongly dictate the overall performance. Additionally, the pitch between

neighboring jets must be accounted for such that the downstream fountain features and entrainment turbulence of one jet do not inhibit proper potential core formation of another.

For the remaining chapters of this manuscript, these important governing parameters will guide the design and development of the direct jet impingement cooler. Minimizing overall height will be prioritized to reduce the volume added by the cooler. Jet locations will be compared to ideal pitch constraints and the nozzle geometry will be chosen based on pressure drop effects.

2.4 REFERENCES

[1] R. J. McGlen, R. Jachuck, and S. Lin, ‘‘Integrated thermal management techniques for high power electronic devices,’’ Appl. Thermal Eng., vol. 24, nos. 8–9, pp. 1143–1156, 2004.

[2] H. Y. Zhang, D. Pinjala and Poi-Siong Teo, "Thermal management of high power dissipation electronic packages: from air cooling to liquid cooling," Proceedings of the 5th Electronics Packaging Technology Conference (EPTC 2003), 2003, pp. 620-625, doi: 10.1109/EPTC.2003.1271593.

[3] C. A. Rubio-Jimenez, S. G. Kandlikar and A. Hernandez-Guerrero, "Numerical Analysis of Novel Micro Pin Fin Heat Sink With Variable Fin Density," in IEEE Transactions on Components, Packaging and Manufacturing Technology, vol. 2, no. 5, pp. 825-833, May 2012, doi: 10.1109/TCPMT.2012.2189925.

[4] T. Wu, B. Ozpineci and C. Ayers, "Genetic algorithm design of a 3D printed heat sink," 2016 IEEE Applied Power Electronics Conference and Exposition (APEC), 2016, pp. 3529-3536, doi: 10.1109/APEC.2016.7468376.

[5] H.-Y. Li, C.-L. Chen, S.-M. Chao, and G.-F. Liang, "Enhancing heat transfer in a plate-fin heat sink using delta winglet vortex generators," International Journal of Heat and Mass Transfer, vol. 67, pp. 666-677, 2013/12/01/ 2013, doi: https://doi.org/10.1016/j.ijheatmasstransfer.2013.08.042.

[6] B. Kwon, T. Foulkes, T. Yang, N. Miljkovic, and W. P. King, "Air Jet Impingement Cooling of Electronic Devices Using Additively Manufactured Nozzles," IEEE transactions on components, packaging, and manufacturing technology (2011), vol. 10, no. 2, pp. 220-229, 2020, doi: 10.1109/tcpmt.2019.2936852.

[7] Q. Zhu et al., "Characteristics of heat transfer and fluid flow in microchannel heat sinks with rectangular grooves and different shaped ribs," Alexandria Engineering Journal, vol. 59, no. 6, pp. 4593-4609, 2020/12/01/ 2020, doi: https://doi.org/10.1016/j.aej.2020.08.014.

[8] R. v. Erp, G. Kampitsis and E. Matioli, "A manifold microchannel heat sink for ultra-high power density liquid-cooled converters," 2019 IEEE Applied Power Electronics Conference and Exposition (APEC), 2019, pp. 1383-1389, doi: 10.1109/APEC.2019.8722308.

[9] D. B. Tuckerman and R. F. W. Pease, "High-performance heat sinking for VLSI," in IEEE Electron Device Letters, vol. 2, no. 5, pp. 126-129, May 1981, doi: 10.1109/EDL.1981.25367.

[10] K. W. Jung et al., "Embedded cooling with 3D manifold for vehicle power electronics application: Single-phase thermal-fluid performance," International Journal of Heat and Mass Transfer, vol. 130, pp. 1108-1119, 2019/03/01/ 2019, doi: https://doi.org/10.1016/j.ijheatmasstransfer.2018.10.108.

[11] M. R. Pais, L. C. Chow, and E. T. Mahefkey, "Surface Roughness and Its Effects on the Heat Transfer Mechanism in Spray Cooling," Journal of Heat Transfer, vol. 114, no. 1, pp. 211-219, 1992, doi: 10.1115/1.2911248.

[12] J. Breitenbach, I. V. Roisman, and C. Tropea, "From drop impact physics to spray cooling models: a critical review," Experiments in Fluids, vol. 59, no. 3, p. 55, 2018/02/26 2018, doi: 10.1007/s00348-018-2514-3.

[13] I. Silverman, A. Yarin, S. Reznik, A. Arenshtam, D. Kijet, and A. Nagler, "High heat-flux accelerator targets: Cooling with liquid metal jet impingement," International journal of heat and mass transfer, vol. 49, no. 17-18, pp. 2782-2792, 2006.

[14] E. N. Wang et al., "Micromachined jets for liquid impingement cooling of VLSI chips," in Journal of Microelectromechanical Systems, vol. 13, no. 5, pp. 833-842, Oct. 2004, doi: 10.1109/JMEMS.2004.835768.

[15] N. Zuckerman and N. Lior, "Jet Impingement Heat Transfer: Physics, Correlations, and Numerical Modeling," vol. 39, G. A. Greene, J. P. Hartnett†, A. Bar-Cohen, and Y. I. Cho, Eds., ed: Elsevier, 2006, pp. 565-631.

[16] H. Martin, "Heat and Mass Transfer between Impinging Gas Jets and Solid Surfaces," in Advances in Heat Transfer, vol. 13, J. P. Hartnett and T. F. Irvine Eds.: Elsevier, 1977, pp. 1-60.

[17] M. Glauert, "The wall jet," Journal of Fluid Mechanics, vol. 1, no. 6, pp. 625-643, 1956.

[18] D. Y. Lee and K. Vafai, "Comparative analysis of jet impingement and microchannel cooling for high heat flux applications," International Journal of Heat and Mass Transfer, vol. 42, no. 9, pp. 1555-1568, 1999/05/01/ 1999, doi: https://doi.org/10.1016/S0017-9310(98)00265-8.

[19] M.-Y. Wen and K.-J. Jang, "An impingement cooling on a flat surface by using circular jet with longitudinal swirling strips," International Journal of Heat and Mass Transfer, vol. 46, no. 24, pp. 4657-4667, 2003/11/01/ 2003, doi: https://doi.org/10.1016/S0017-9310(03)00302-8.

3. THERMAL AND ELECTRICAL PERFORMANCE IN HIGH-VOLTAGE POWER MODULES WITH NONMETALLIC ADDITIVELY MANUFACTURED IMPINGEMENT COOLERS

Co-Authors: David Huitink, Asif Emon, Amol Deshpande, and Fang Luo

ABSTRACT

As high voltage, wide-band-gap power modules increase in power density with high switching frequency, they create localized hot spots and harmful electromagnetic interference. If not treated properly, these issues can drastically reduce the reliability of the devices. In this paper, we propose a solution to address both of these challenges created by power module building blocks which are designed for use in a hybrid-electric aircraft traction inverter. Additive manufacturing is used to fabricate a non-metallic jet impingement device to decrease power module temperatures. Moreover, the non-metallic structure limits the accentuation of electromagnetic interference created by the module operating at high switching frequencies. Conjugate heat transfer simulations are used to predict the thermal performance of the cooler. In this study, a reduction of maximum die temperatures is observed, along with an increase in temperature uniformity throughout the base plate. Experimental results show a minimum thermal resistance of 0.1K/W and an average heat transfer coefficient up to 3600 W/m2.K at peak operation. Finally, electromagnetic interference tests are performed to show a two orders of magnitude reduction of parasitic capacitance using the non-metallic cooler compared with a metallic heat sink. This directly leads to a 25 dB decrease in the common mode noise.

INDEX TERMS

Direct cooling, inverter, jet impingement, liquid cooling, nonmetallic, polymer, power module, 3D printing

NOMENCLATURE

W	Watts
K	Kelvin
EMI	Electromagnetic interference
AMHS	Additively manufactured heat spreader

3.1 LITERATURE REVIEW

As energy demands and electrification of the transportation sector continue to increase, new power electronic innovations are becoming necessary. With respect to high switching losses, thermal management techniques are reaching the limit of feasibility with respect to size, cooling capacity and weight. Additionally, as our electric grid continues to consume large amounts of power, smart energy storage and conversion are demanding more reliable power electronics. Moreover, with the internal combustion engine in the transportation sector producing 25-30% of all greenhouse gases [1], industrial leaders and governments are pushing towards a rapid integration of renewable resources [2]. Therefore, as external pressure is put on the transportation industry, electric and hybrid-electric vehicles such as automobiles and aircraft must incorporate reliable power electronics containing high power density [3]. Moreover, rapid growth of the renewable energy sector, such as solar and energy storage, have intensified the need for high performance power electronics [4]. However, while wide bandgap materials offer benefit in such systems, often power module packaging limits the potential gains based on thermal management and reliability concerns in high power dense systems. Significant electro-thermally coupled design challenges face this technology adoption, as improper thermal management can lead to thermal runaway and device degradation, which may worsen due to non-uniform cooling [5]. Moreover, a

high voltage switching induced common mode noise burdens circuit components and drives un-reliability [6].

Traditionally, cold plates, heat sinks and heat pipes are the tools of choice for electronic cooling. However, to combat these new thermal challenges, significant research efforts have sought to develop and demonstrate high heat-flux thermal systems with low volumetric footprints. Novel solutions have been proposed to achieve higher cooling rates where typical systems may be deficient. Methods such as microchannels, spray cooling and jet impingement cooling have been presented as high heat-flux solutions. Literature reviews have catalogued numerous studies with heat flux performance achieving 1000 W/cm2 with single-phase cooling techniques [7]. Microchannels have offered high heat transfer directly integrated on the backside of a chip, while maintaining low volume requirements. For example, Hirshfeld et al. demonstrated a microchannel cooler with heat fluxes up to 1430 W/cm2 [8]. Tuckerman and Pease additionally demonstrated high heat flux values in the range of 790 W/cm2 in planar integrated circuits. However, the small hydraulic diameters of the channels present high pressure drop values. This has the effect of introducing additional pumping requirements as well as creating stress in the system, taxing the effective performance and reliability of the combined thermo-electronic device [9].

Spray cooling is a second type of single-phase cooling that has gained traction for power electronics thermal management. While high heat flux values can be achieved, there are common issues associated with such systems. First, the nozzle sizes required to achieve the highest performance with “atomized” liquid are prone to clogging and erosion. Secondly, the required driving pressure necessary to perform spray cooling may be unrealistic for real-world scenarios [9]. Those who have successfully shown the heat flux performance of spray cooling demonstrate values up to 1200 W/cm2 [10].

Jet impingement cooling is widely used to create localized zones with extremely high heat transfer coefficients. While this technique can be useful for systems such as chips and modules, the larger size can generate intense pressure drops. Therefore, this method is known to be erosive and damaging due to the higher flow rates and pressure occurred at the impingement nozzles and manifolds [11]. Regarding performance, Overholt et. al. demonstrated a metallic micro-jet cooler with heat flux values up to 1500 W/cm2[12]. Browne et. al. developed a Si impingement device with a heat flux of 930 W/cm2 [13]. And additionally, Sharma et. al. machined micro-jets into polyphenylene sulfide to create a non-metallic cooler with 150 W/cm2 capacity [14].

While these cooling methods offer great thermal performance in high heat flux applications, they have opportunities to be optimized to reduce their effects of common mode noise generation. In one example, Wei et. al. reported a non-metallic, chip-scale impingement cooler fabricated using conventional machining techniques [15]. They demonstrate thermal resistance values as low as 0.25 K/W, for chips domains of 14 x 14 mm2, illustrating how such techniques can offer sufficient cooling if properly designed and integrated.

Yet, rarely are the impacts of electromagnetic interference (EMI) considered in thermal management designs. For power electronics, the parasitic capacitance is the measure of electronic noise between a power module, the thermal management device and ground. Conventional heat sinks and other metallic cooling systems provide a pathway by which common mode noise can be accentuated by the metallic structure between the power module and ground. Therefore, if one can exchange the metallic structure for a non-conductive system, the low-frequency common mode noise can be reduced [16]. Thus, it is this challenge which drives the premise of the non-metallic structure. It is the domain size of the power module hot spots which motivates the choice to utilize large-scale jet impingement. And it is the readily available nature of additive manufacturing that

brings these two design features into a customizable, directly integrable thermal management solution.

In this work, a multi-functional cooling system, made with internal manifold channels, jet impingement zones and heat spreading outlet paths work to reduce maximum device temperatures and limit extreme thermal gradients. Herein, we describe the manufacture and performance of this device, in terms of thermal and electrical FEA predictions at the device and system level for a high voltage power module (CREE CAS325) as well as lab experimental validations of the heat removal performance. A loop containing a centrifugal pump, turbine flow meter, pressure transducers and thermistors are utilized to obtain pressure and temperature drops across a test section to extract heat transfer coefficients and thermal resistance values.

3.2 DESIGN

The primary goal of the AMHS device is to create a localized hot-spot cooler for power modules in a non-metallic structure through convective heat transfer. The hot-spot cooling can lower maximum die temperatures and increase module temperature uniformity through direct jet impingement. The non-metallic construction reduces weight and limits the parasitic capacitance generated between the power module and system ground. Furthermore, inside the new device custom designed manifolds and outlets paths can provide excellent heat spreading in a low-pressure drop platform. With a single inlet and outlet, fastener allocations and a smooth top surface for sealant, the device is directly integrable with a novel high-powered inverter designed for use in hybrid-electric propulsion systems.

The design process of the cooler was broken down into two main tasks: nozzle design and manifold coolant delivery optimization. First, great care must be taken to ensure the jet impingement zone is properly designed. Therefore, using correlations identified from literature

[21], the nozzle shape, pitch and nozzle-to-plate spacing were designed to fit well-established parameters. Next, the manifold was created to encourage minimal pressure loss in the high-pressure side routing, then optimized in CFD to obtain pressure balanced nozzle inlet so as to obtain temperature balancing across hot spot arrays.

The internal manifold structure distributes incoming coolant to the jet impingement nozzles, Fig. 1a, where it then passes through the nozzles and impinges onto the critical hot-spot areas, Fig. 1b. The fluid then provides additional cooling by passing over the heated surface through the placement of lateral outlet paths. Finally, the coolant recollects inside the device and exits in a single outlet channel, Fig. 1c. Moreover, Fig. 1d gives a top-view of the device, defining the relationship between the position of the dies and the jet impingement location.

3.3 MANUFACTURING

The AMHS device is manufactured using fused deposition modelling (FDM) 3D printing. Using ABS plastic as the build material, the new device has the benefit of being low cost, light-weight and be rapidly prototyped. However, FDM printing creates inherently rough surfaces through the fusing of material layers. For internal flow geometries, these surface defects have the potential to create large pressure drops and interfere with the jet-impingement cooling performance. To combat these rough features, ABS “smoothing” can be achieved using acetone vapor contact, since ABS is soluble in acetone.

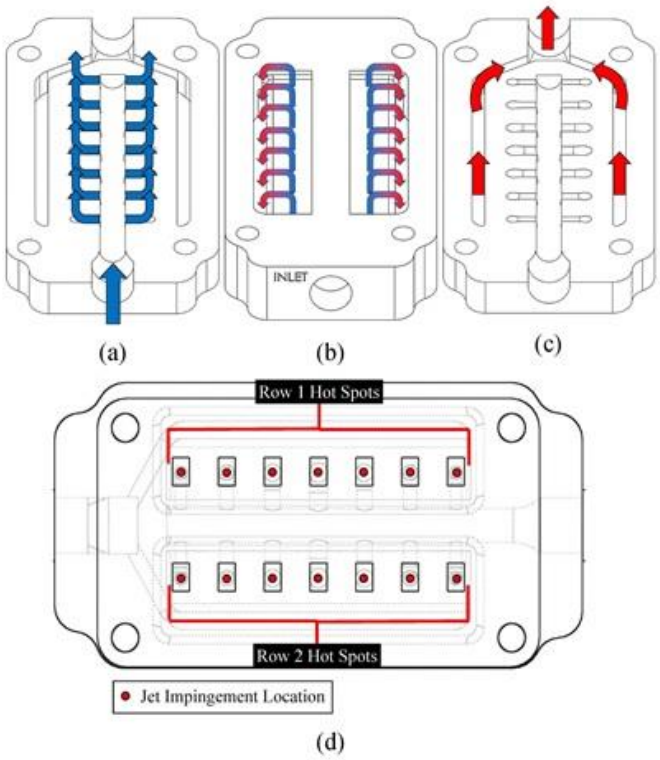

Figure 1: a) Coolant enters the device and is distributed to using a manifold. b) Fluid passes through the nozzles and impinges onto critical areas before exiting through lateral outlet paths. c) The coolant recollects inside the device and exits. d) Top-view showing the die positions (hot-spots) relative to the jet impingement locations.

When ABS comes into contact with liquid and/or vapor acetone, the plastic dissolves at the surface, and the surface becomes smooth through material re-deposition in the recessed valleys created by the FDM process. Before smoothing, the surface contains systemic roughness around 80 microns, peak to trough, in accordance with the nozzle characteristics. However, after vapor smoothing, we see a 90% reduction in surface roughness (Ra). Additionally, the act of smoothing the ABS surface as the added benefit of creating a non-permeable surface. Without smoothing, internal liquid can seep through the FDM layers. However, the chemical vapor smoothing prohibits this effect with sealed surfaces.

3.4 COOLING PERFORMANCE PREDICTION VIA FEA

To simulate the heat removal capability of the AMHS, a coupled solution of conjugate heat transfer and computational fluid dynamics is utilized. Using ANSYS FLUENT, three power module representations are placed on an aluminum base plate, whereon a standard cold plate is placed to compare against three AMHS devices placed beneath each module. Fig. 2a depicts the power modules, with each containing 14 individuals heat input locations. Moreover, Fig. 2b illustrates how three AMHS devices were placed on the base plate, with the purpose of each jet location impinging directly beneath a single hot spot die location. These locations provide a representation of the design of the CREE CAS325 power module. For this simulation, a total wattage is assigned to each device and uniformly divided among the heat locations in the form of volumetric heat generation. The importance of constructing the model to mimic such heat inputs is to correctly assess the performance of the jet impingement locations and if the necessary thermal gradients between critical locations are reduced. Furthermore, modules 1 and 2 each produce a total of 715 watts, giving a power density of 16.6 W/cm2, Module 3 produces 550 watts, or 12.8 W/cm2. The layout and selection of the power module layout and power distribution represent the physical arrangement of a novel, 3-level T-type inverter with the design purpose of being implemented in hybrid electric propulsion systems.

Regarding the fluid dynamics boundary conditions, a zero-pressure outlet is considered, with an inlet flow rate of 2 GPM at 20 C. All exposed outside surfaces are considered adiabatic. For the AMHS, conduction is considered between the base plate and the cooling device surface with the presence of thermal interface material between metallic surfaces such as the base plates and modules. Furthermore, convection is simulated at the fluid-to-base plate interface for the purpose of capturing heat removal through directed cooling. In the cold plate simulation,

conduction is also considered at the base plate interface, with convection occurring at the fluid-to-tube internal surface of the cold plate.

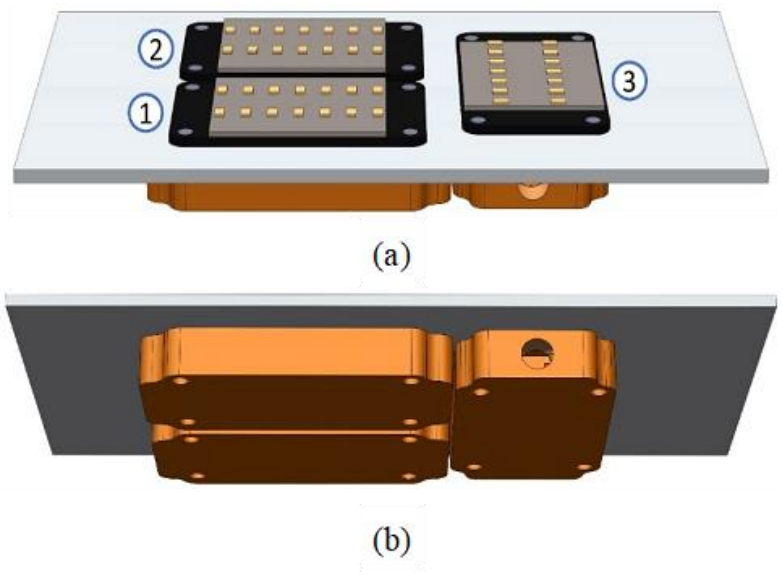

Figure 2: a) power module arrangement with corresponding callouts. b) depiction of three AMHS devices, with each directly impinging onto the power module die locations.

The CFD results indicate that the AMHS cooling scheme provides a 7 °C reduction of maximum temperature in each die location compared to the cold plate arrangement. The cold plate and AMHS cooling results are given in Figure 3a and 3b, respectively, as they provide thermal management to module 1. As seen, the cold plate generates an extensive parabolic thermal profile along the two rows of dies, indicating a large co-heating effect. Additionally, there are temperature variations not only along the length of die rows, but across the two rows themselves. The coolant enthalpy rises as it passes through the cold plate and cools the modules, thus row two experiences better cooling due to lower coolant temperatures. Moreover, we see a 0.5ºC temperature difference between the two outer die locations, further confirming the presence of large thermal gradients with the cold plate cooling. On the contrary, the AMHS device produces a thermal profile with negligible temperature discrepancies across the die rows, nor along them.

Without directed cooling, the internal dies will see an increased temperature compared to the outer locations due to the co-heating effect. This temperature imbalance may cause unbalanced lifetimes in the devices regarding thermally-driven reliability failure modes such as degradation and interconnect fatigue, as well as drive current imbalances due to conduction resistance increase with temperature. As seen, the cold plate lacks the ability to target the hot spots and adequately prevent co-heating. However, in the AMHS, the custom-designed manifold can control the volumetric flow rate through each nozzle to create a linear temperature profile in the module in the longitudinal direction.

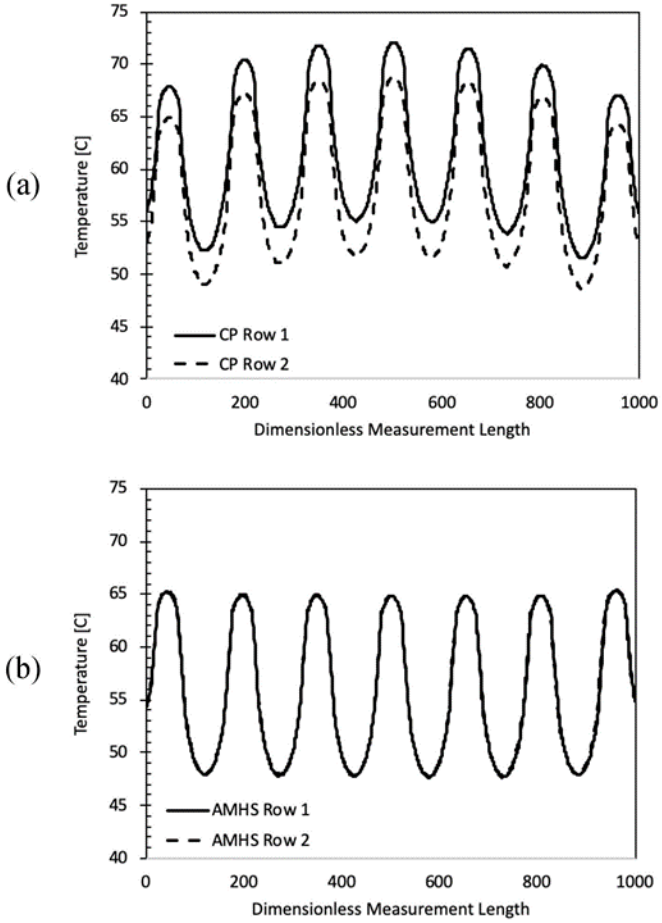

Figure 3: Temperature profiles along two rows of die with the a) cold plate and b) AMHS device.

Lastly, before carrying out the simulations it was theorized that relying on localized impingement cooling would increase the average module temperature compared to the cold plate. By focusing the cooling on a hot-spot, the intense temperature gradients would be limited; however, a drawback would be the lack of cooling on the remaining exposed module surface, therein creating egresses for temperature spreading. Due to the presence of thermal interface layers, the simulation results show the opposite effect, as seen in Fig. 4a, in addition to Fig. 4b which shows the maximum junction temperatures in each module. Across each module, the AMHS produces an average temperature that is 1- 4.0 °C lower than the cold plate. Moreover, the comparison of maximum junction temperatures provides insight into how efficient the directed cooling targets the die hot spots, with greater accentuation of this effect is module 1.

In general, when determining the successfulness of the new cooling scheme compared to a traditional cold plate, overall electronic reliability is the deciding factor. By directing the coolant fluid directly into the power module hot spots, the critical die locations can experience lower maximum temperature. And through custom-designed manifold channels and nozzles, temperature uniformity is maintained, improving electrical and thermomechanical balancing across device sites.

To validate the temperature differences between paralleled dies, an experimental heating block design was fabricated. The heating block is capable of emulating the same die layout in the employed power module in the manuscript by creating localized hot spots. Individual temperature measurements are then taken on each hot spot and the thermal profiles can be recorded. More details on the setup can be found in a previous article by the same authors [22]. The results of this preliminary experiment in Fig. 5 show similar variances across rows of die in the simulated and experimental thermal profiles.

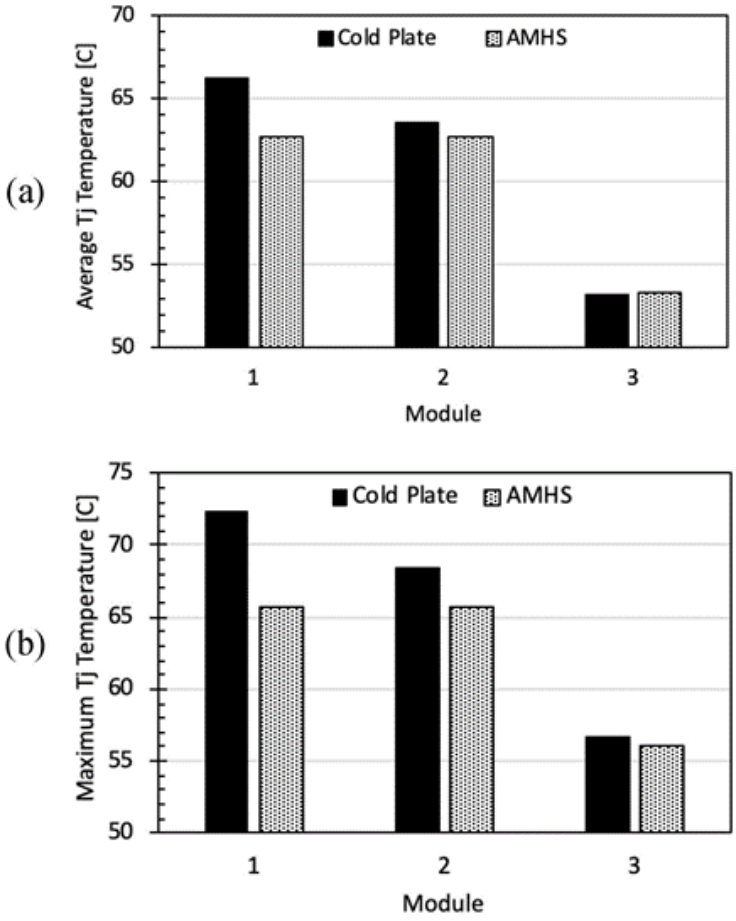

Figure 4: a) Average simulated power module temperatures showing an increase with localized cooling. b) Maximum temperatures showing a decrease in module 1, with modules 2 and 3 showing negligible differences.

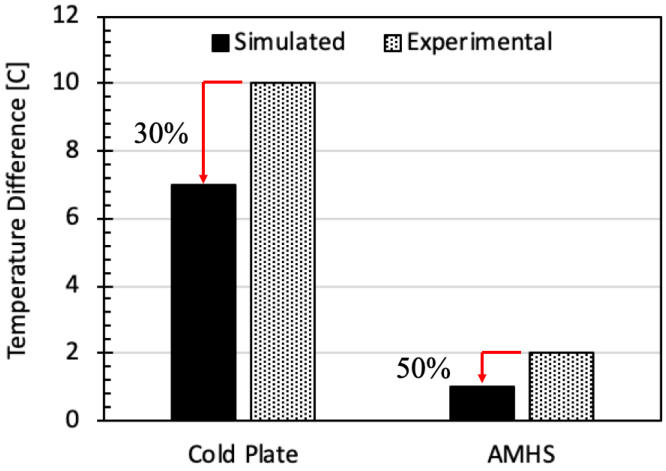

Figure 5: Simulated versus experimental temperature difference between paralleled dies.

3.5 EXPERIMENTAL THERMAL VALIDATIONS

To validate the cooling system performance in terms of heat removal capacity and pumping losses, an experimental test bed has been developed consisting of a flow loop, heating elements and an external chiller. Thus, it represents a closed-loop cooling system in which the working fluid is isolated from the chiller loop. The flow loop specifications are given in Table 1, including sensor accuracy, flow rate capacity and chiller operating ranges. To represent a power module during operation and provide a proof of concept evaluation, two resistive strip heaters are used to replicate hot-spots on a power module with two rows of switching dies. With a maximum input wattage of 300 W, the system has the capacity to replicate modules during normal operation. Fig. 6 gives a representation of a single AMHS device attached to a base plate, on which two heaters have been placed with insulation covering the exposed surfaces. Additionally, thermocouples are placed on the base plate to obtain an average plate temperature during operation.

TABLE 1
EXPERIMENTAL SETUP: FLOW LOOP

Component	Characteristics
Pressure Transducers	± 0.005 PSI
Thermistors	±0.2 °C
Centrifugal Pump	0.1 – 2.5 GPM
Recirculating Chiller	± 0.1 °C
Power Meter	± 1.0% V
Resistive Heaters	0 – 300 W @ 120VAC
K-Type Thermocouple	± 1.0 °C

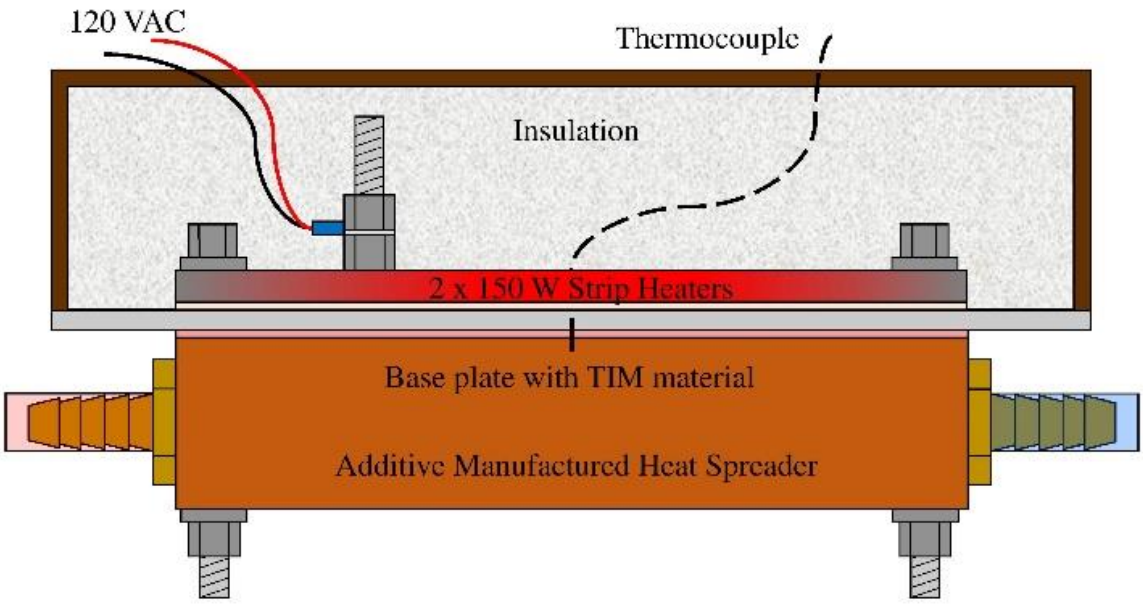

Figure 6: Thermal setup including strip heaters, thermocouples and the AMHS device.

The required pumping power is given as Equation

$$P_{pump} = \dot{V} \cdot \Delta P \tag{1}$$

where ΔP is the pressure difference between the inlet and outlet of the cooling device and $\dot{V}$ is the volumetric flow rate [19]. This relationship allows one to correlate the thermal management performance of the device with the pressure drop associated with the design.

The two heat transfer metrics utilized in this study are the thermal resistance and heat transfer coefficient. First, thermal resistance is given as

$$R_{th} = \frac{T_{plate} - T_{fluid}}{P_{input}} \tag{2}$$

where T_{plate} is the average base plate temperature, T_{fluid} is the average working fluid temperature, and P_{input} is the power supplied to the resistive heaters [20]. Next, the overall heat transfer coefficient of the thermal management device is

$$h_{coeff} = \frac{1}{A_{eff} \cdot R_{th}} \tag{3}$$

where A_{eff} is the effective heat transfer area between the cooling system and the base

plate. The coolant power removal is determined by

$$Q = \dot{m} \cdot C_p \cdot \Delta T \tag{4}$$

where ΔT is the temperature difference between the inlet and outlet of the cooling device.

Using these relationships, the performance of the AMHS can be evaluated with respect to its ability remove substantial heat loads in a simulated power module. During testing, resistive heater power levels were increased from 100 to 250 W in 50 W increments. First, the viability of the testing insulation needed to be confirmed. Fig. 7 gives the power removed by the AMHS device at each testing wattage. As seen, the percent loss between the expected and actual heat removal levels range between 1 – 20%, with an average loss of 8%. This confirms that on average, 92% of the input power is seen by the cooling device and that the experimental setup provides repeatable boundary conditions to replicate a power module.

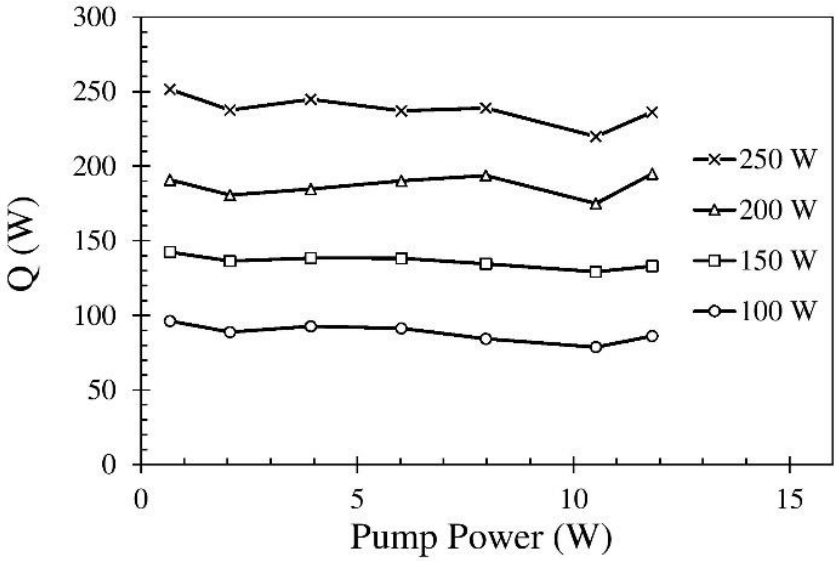

Figure 7: Plot of the power removed by the AMHS to confirm a viable and repeatable testing setup.

Additionally, during testing with the AMHS device, the heaters and base plate reached thermal steady state quicker than the cold plate setup. The large metallic volume of the cold plate

must reach thermal equilibrium with more thermal mass than the lightweight, non-metallic structure of the localized cooler. Therefore, more time is required for the cold plate.

Next, the thermal resistance between the working fluid and the heater-to-plate surface is plotted against the required pumping power. As seen in Fig. 8a, the thermal resistance is 0.3 at 0.1 W and begins to reach a plateau at 10 W with a resistance value of 0.1 K/W. Additionally, across the four power levels, the AMHS device produces consistent performance with the resistance showing a maximum percent difference of 15%. The heat transfer coefficient is closely related to the thermal resistance, as seen in (3). This additional metric further correlates the thermal management performance with the physical dimensions of the AMHS by included the effective cooling area. In the first design, the AMHS relies not only on jet impingement for heat removal, but also on the lateral outlet paths that contribute to additional performance through cross flow effects. Therefore, the combination of the jet impingement zones and cross-flow interactions must be considered into the effective area. Fig. 8b presents the effective heat transfer coefficient of the AMHS across four input power levels and CP at 200 W.

As expected, the heat transfer coefficient slope gradually decreases as the pump power increases, with an average maximum value of 3700 W/m2□K. Combining this with the low thermal resistance of 0.1 K/W, the AMHS proves to be an efficient thermal management device at the power-module level, even with ample room for optimization for pumping losses and jet locations. And while this reported HTC is not quite as large as those reported in some other methods, the values reported here are normalized across 2600 mm2, conveying the sense of an effective heat removal based on contact area of the baseplate with the coolant. As a result, the local heat transfer coefficient at the stagnation zone of one jet is estimated to be 53,000 W/m2*K, using Equation 50 for Pr > 3, in [17]. Compared against the simulated results which give a maximum

HTC of 47,000 W/m2*K, the correlation is reasonable. Moreover, this technique avoids some of the pitfalls of clogging and system requirements associated with the high HTC methods like microchannel and spray cooling.

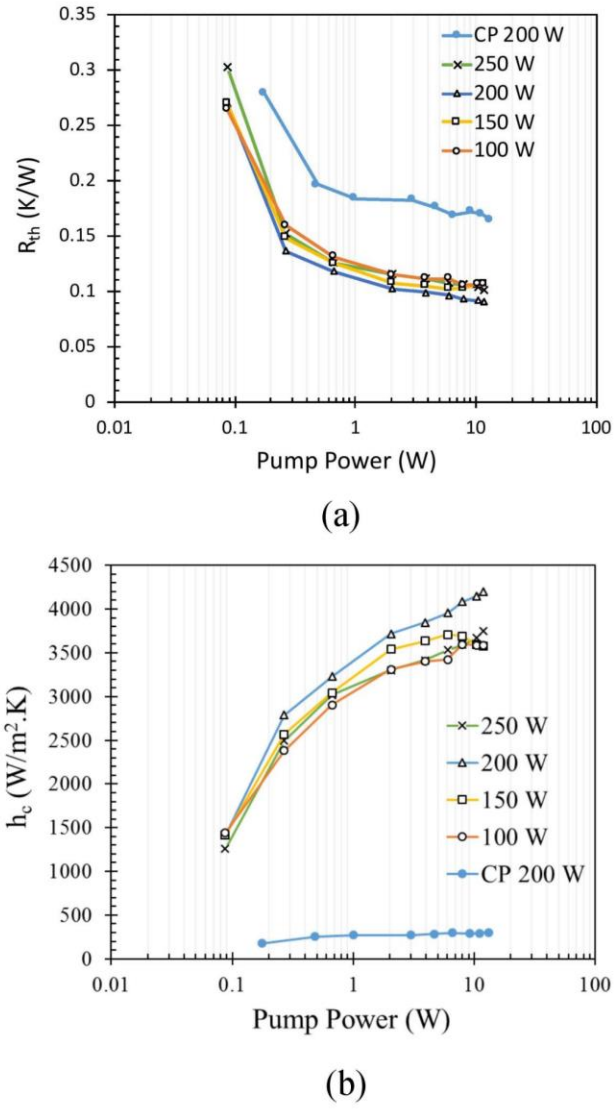

Figure 8: a) Thermal resistance vs. pump power showing a performance plateau at 10 W. b) Heat transfer coefficient vs. pump power showing an increasing trend with a gradual plateau at 10 W of input power.

3.6 EFFECTS OF MATERIALS ON EMI

Beyond its thermal performance, the AMHS integration into a high voltage, high frequency switching inverter system has important implications for inductive coupling with the power

MOSFET currents. By moving away from metallic cold plates to additively manufactured ABS plastic jet impingement thermal management. The polymeric material offers both weight and EMI benefits. Having a reduced ABS plastic dielectric constant of 2.0 – 3.5, the non-metallic construction offers resilience to these coupling effects, and can reduce damaging EMI noise. To evaluate these effects a half-bridge module is used to simulate the parasitic capacitance between a MOSFET switching node (marked as AC) and the power ground of a power module. The capacitance value is influential in the creation of common mode electromagnetic interference (CM EMI). Therefore, it can be directly inferred and calculated that a reduction in capacitance can directly reduce the amount of harmful EMI capacity.

Using ANSYS Q3D to extract the parasitic capacitance, the relationship between the heat sink material and the CM noise can be found. Fig. 9a displays the model utilizing the new AMHS as the cooling device. With a half-bridge module attached to a DBC layer and base plate, the model can simulate the interaction between layers, in addition to the effects of the thermal management device. Tests were also performed with a conventional aluminum heat sink attached to the base-plate. Fig. 9b and Fig. 9c present the resulting parasitic capacitance across the conventional heat sink and AMHS device, respectively. In comparison, the metallic heat sink creates a capacitance value that is two orders of magnitude larger than that of the non-metallic material. Because the ABS plastic contains a lower dielectric constant, there exists a reduced feedback loop with the AMHS device than the metallic heat sink. This is the same feedback loop that drives the intensity of common mode noise seen in the half-bridge power module. Therefore, the AMHS device results in a 60dB attenuation in the simulated common mode noise in the 100kHz – 100MHz range as compared to the metallic heat sink.

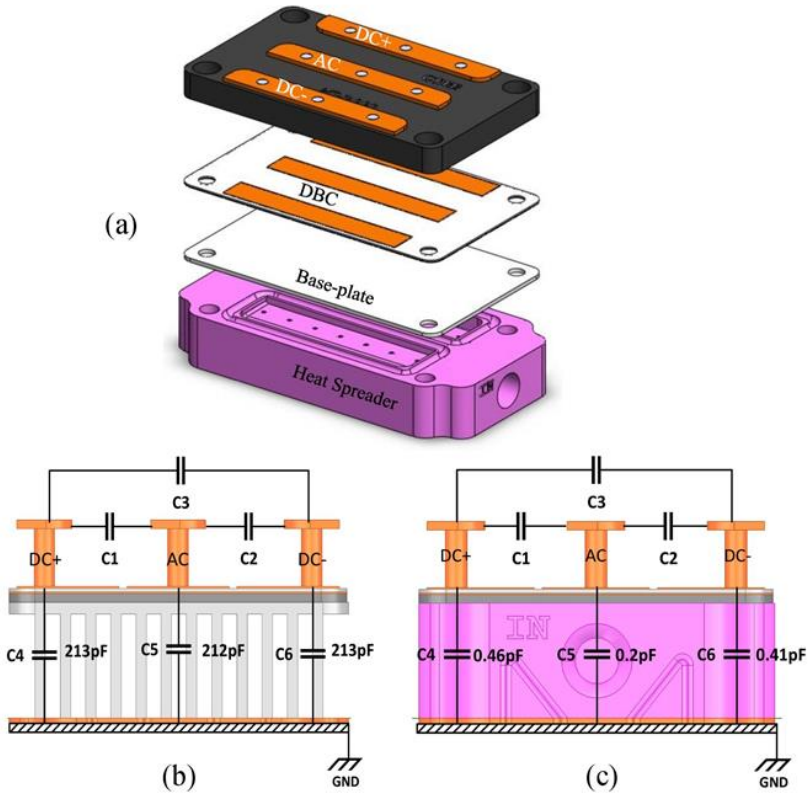

Figure 8: a) ANSYS Q3D model to extract the parasitic capacitance between the non-metallic heat spreader and an aluminum heat sink. b) Parasitic capacitance model of a half-bridge module and metallic heat sink. c) Parasitic capacitance model of a half-bridge module and the non-metallic AMHS device.

This was experimentally validated in Fig. 10 and though while not quite 60dB reduction, an impressive 25dB noise reduction was observed in the same frequency range. Finally, Figure 11 displays the experimental common mode current response with the two cooling systems to provide validation of the improved EMI performance. As we can see, the experimental waveform of CM current sees a decrease in noise at the point of a given pulse. This is a direct result of the reduced parasitic capacitance between the power module and ground with the AMHS cooler. Thus, we see a damped response in CM current.

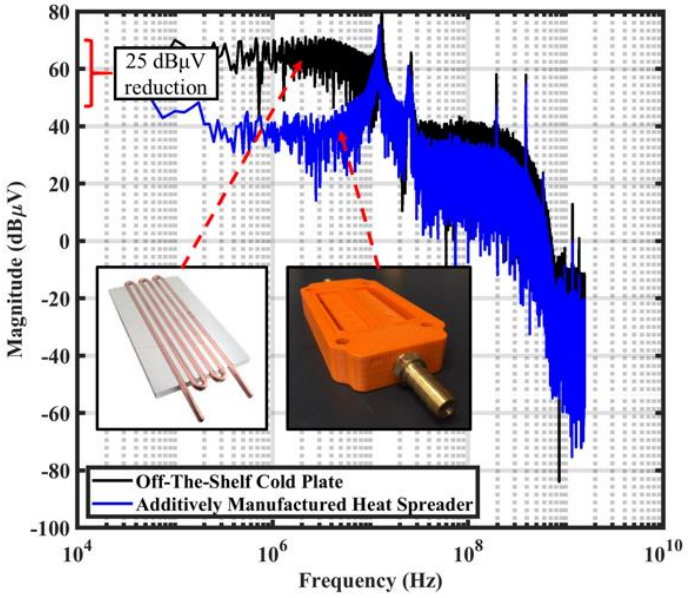

Figure 9: Comparison of common mode noise accentuated by an off-the-shelf cold plate versus the AMHS device.

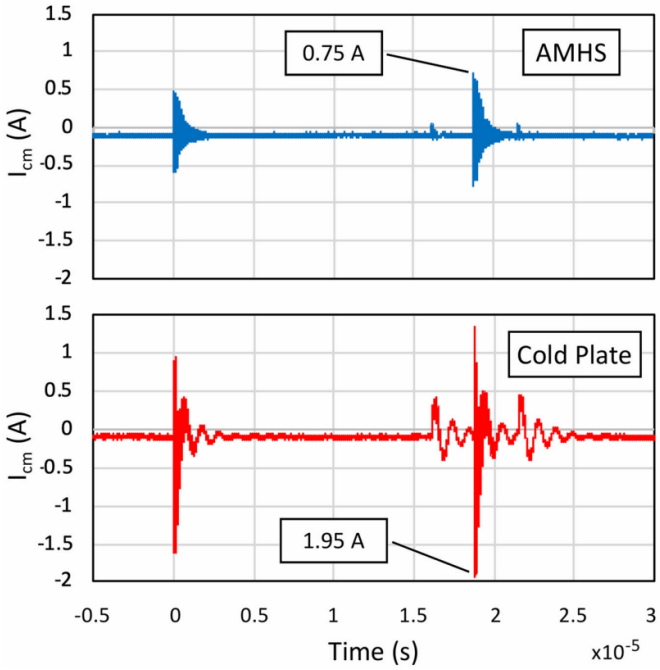

Figure 10: Comparison of experimental common mode current with the cold plate and AMHS assemblies.

3.7 CONCLUSION

The simulated and experimental performance of the additively manufactured heat spreader show an increase in heat transfer, while minimizing the effects of common mode noise. The jet impingement design can successfully target the hot spots located in a typical power module by decreasing maximum temperatures and increasing the temperature uniformity along the die locations. Moreover, the required pumping power ranges from 0.1 – 10 W, depending on flow rate, with moderate pressure drops across the device. The experimental setup proved a lower thermal resistance between the heat source and the working fluid in the AMHS when compared to an off-the-shelf cold plate. Additionally, the directed coolant provided a heat transfer coefficient up to 3700 $W/m^2 \cdot K$. Lastly, the simulated EMI testing was implemented to determine the effect of the non-metallic composition as compared to a traditional cold plate.

The results show a two orders of magnitude reduction of parasitic capacitance, leading to a 25dB reduction of experimental common mode noise across the line impedance stabilization network. These remarkable improvements in EMI performance suggest that a significant reduction in the required EMI filtering could greatly impact the total inverter volume, leading to much improved power density. In fact, the move from a metallic cold plate to a polymer printed heat spreading element already improves the effective system specific power by ~20x, based on the weight reduction by material choice. Coupled with the additional reduction in EMI filtration, these gains offer significant advantage for size and weight reduction in mobile or aircraft traction systems. Moreover, these EMI benefits were achieved with simple polymers, which could be doped with magnetic content for further improvements in EMI shielding effects, for even greater result.

In regard to the applicability of the cooler, important considerations must be looked at further. First, the durability of the non-metallic material must be evaluated. Conventional methods for liquid cooling use aluminum and copper which have well-defined flow rate parameters for maximum longevity. On the contrary, little study has been performed about erosion rates in additive manufactured materials. Secondly, the cost of the cooler versus design customization for hybrid-electric propulsion systems will be a large contributing factor. Lastly, system-wide grounding considerations must be made with respect to coolant loops. With cold plates and heat sinks, there exists a pathway for current to be grounded and exit the system. With the new non-metallic design, there exists an opportunity for the coolant to become energized and cause harm to the electrical devices.

Regardless of the required further development of the technology, additive technologies offer a wealth of opportunity in the development of high-power dense electronics, from packaging to system level thermal management as described herein. As the manufacturing technology continues to improve and lower in cost, the ability to provide custom solutions in power systems may be the key in delivering multi-functional system components for the next generation of high power, high voltage electronic packages.

3.8 ACKNOWLEDGEMENT

This work was supported by the National Science Foundation Engineering Research Center for Power Optimization of Electro-Thermal systems (POETS) with cooperative agreements EEC-1449548. Any opinions, finding, and conclusions or recommendations expressed in this material are those of the author(s) and do not necessarily reflect the views of the National Science Foundation.

3.9 REFERENCES

[1] K.V. Singh, H.O. Bansal and D. Singh, "A comprehensive review on hybrid electric vehicles: Architectures and components," *Journal of Modern Transportation*, vol. 27, no. 2, pp. 77-107, June 2019.

[2] S.E.I. Association, "Solar industry letter to congress: Extend the ITC," 2019. https://www.seia.org/sites/default/files/2019-07/SEIA-ITC-Signon-Letter-July2019.pdf.

[3] S. Jafari and T. Nikolaidis, "Thermal management systems for civil aircraft engines: Review, challenges and exploring the future," *Applied Sciences*, vol. 8, no. 11 2018.

[4] G. Wang, G. Konstantinou, C.D. Townsend, J. Pou, S. Vazquez, G.D. Demetriades and V.G. Agelidis, "A review of power electronics for grid connection of utility-scale battery energy storage systems," *IEEE Transactions on Sustainable Energy*, vol. 7, no. 4, pp. 1778-1790 2016.

[5] J. Hernandez-Ambato and C. Pace, "Embedded mini-Heater design for power loss remote measurement and thermal runaway control on power devices for Accelerated Life Testing," in , 2016, pp. 1-6.

[6] F. Zare, D. Kumar, M. Lungeanu and A. Andreas, "Electromagnetic interference issues of power, electronics systems with wide band gap, semiconductor devices," in , 2015, pp. 5946-5951.

[7] M.A. Ebadian and C.X. Lin, "A review of high-heat-flux heat removal technologies," *Journal of Heat Transfer-Transactions of the Asme*, vol. 133, no. 11, pp. 11, November 2011.

[8] H. Hirshfeld, I. Silverman, A. Arenshtam, D. Kijel and A. Nagler, "High heat flux cooling of accelerator targets with micro-channels," *Nuclear Instruments & Methods in Physics Research Section a-Accelerators Spectrometers Detectors and Associated Equipment*, vol. 562, no. 2, pp. 903-905, Jun 2006.

[9] D. Sharar, N. Jankowski and B. Morgan, *Review of Two-phase Electronics Cooling for Army Vehicle Applications*, 2010.

[10] M.R. Pais, L.C. Chow and E.T. Mahefkey, "Surface roughness and its effects on the heat transfer mechanism in spray cooling," *Journal of Heat Transfer*, vol. 114, no. 1, pp. 211-219 1992. http://dx.doi.org/10.1115/1.2911248.

[11] J. Broughton, V. Smet, R.R. Tummala and Y.K. Joshi, "Review of thermal packaging technologies for automotive power electronics for traction purposes," *Journal of Electronic Packaging*, vol. 140, no. 4, pp. 11, December 2018.

[12] M. Overholt, A. McCandless, K. Kelly, C. Becnel and S. Motakef, *Micro-Jet Arrays for Cooling of Electronic Equipment*, 2005.

[13] E.A. Browne, G.J. Michna, M.K. Jensen and Y. Peles, "Microjet array single-phase and flow boiling heat transfer with R134a," *International Journal of Heat and Mass Transfer*, vol. 53, no. 23,pp. 5027-5034 2010.

[14] C.S. Sharma, G. Schlottig, T. Brunschwiler, M.K. Tiwari, B. Michel and D. Poulikakos, "A novel method of energy efficient hotspot-targeted embedded liquid cooling for electronics: An experimental study," *International Journal of Heat and Mass Transfer*, vol. 88, pp. 684-694 2015. http://www.sciencedirect.com/science/article/pii/S0017931015004159.

[15] T. Wei, H. Oprins, V. Cherman, J. Qian, I.D. Wolf, E. Beyne and M. Baelmans, "High-efficiency polymer-based direct multi-jet impingement cooling solution for high-power devices," *IEEE Transactions on Power Electronics*, vol. 34, no. 7, pp. 6601-6612 2019.

[16] H. Zhang and A. Wu, "Common-mode noise reduction by parasitic capacitance cancellation in the three-phase inverter," *IEEE Trans.Electromagn.Compat.*, vol. 61, no. 1, pp. 295-300 2019.

[17] X. Liu, J.H, Lienhard and J.S Lombara, "Convective heat-transfer by impingement of circular liquid jets," *J.Heat Transf.-Trans.ASME*, vol. 113, no. 3, pp. 571-582, AUG 1991.

[18] R. Whitt, B. Nafis, D. Huitink, Z. Yuan, A. Deshpande, B. Narayanasamy and F. Luo, "Heat Transfer and Pressure Drop Performance of Additively Manufactured Polymer Heat Spreaders for Low-Weight Directed Cooling Integration in Power Electronics," in, 2019, pp. 451-455.

[19] T.W. Wei, H. Oprins, V. Cherman, E. Beyne and M. Baelmans, "Experimental and numerical investigation of direct liquid jet impinging cooling using 3D printed manifolds on lidded and lidless packages for 2.5D integrated systems," Applied Thermal Engineering, vol. 164, pp. 1145352020. http://www.sciencedirect.com/science/article/pii/S1359431119344060.

[20] Y. Cengel, Heat and mass transfer: fundamentals and applications, McGraw-Hill Higher Education, 2014.

[21] N. Zuckerman and N. Lior, "Jet impingement heat transfer: Physics, correlations, and numerical modeling," Advances in Heat Transfer, vol. 39, pp. 565-631 2006. http://Www.Sciencedirect.Com/Science/Article/Pii/S0065271706390065.

[22] Reece Whitt And David Huitink (2019) Thermal Validations Of Additive Manufactured Non-Metallic Heat Spreading Device For Hot Spot Mitigation In Power Modules. International Symposium On Microelectronics: Fall 2019, Vol. 2019, No. 1, Pp. 000398-000403.

4. ADDITIVE MANUFACTURED IMPINGING COOLANT, LOW ELECTROMAGNETIC INTEFERENCE, AND NONMETALLIC HEAT SPREADER: DESIGN AND OPTIMIZATION

Co-Authors: Skyler Hudson, David Huitink, Zhao Yuan, Asif Emon and Fang Luo

ABSTRACT

With the increase of electronic device power density, thermal management and reliability are increasingly critical in the design of power electronic systems. First, increased density challenges the capability of conventional heat sinks to adequately dissipate heat. Secondly, higher frequency switching in high voltage, high current, wide bandgap power modules is creating intensified electromagnetic interference challenges, in which metallic heat removal systems will couple and create damaging current ringing. Furthermore, mobile power systems require lightweight heat removal methods that satisfy the heat loads dissipated during operation. In this effort we introduce an additive manufacturing pathway to produce custom heat removal systems using non-metallic materials, which take advantage of impinging fluid heat transfer to enable efficient thermal management. Herein, we leverage the precision of AM techniques in the development of 3D optimized flow channels for achieving enhanced effective convective heat transfer coefficients. The experimental performance of convective heat removal due to liquid impingement is compared with conventional heat sinks, with the requirement of simulating the heat transfer needed by a high voltage inverter. The implementation of non-metallic materials manufacturing is aimed to reduce electromagnetic interference in a low weight and reduced cost package, making it useful for mobile power electronics.

NOMENCLATURE

AM	Additive manufactured
AMHS	Additive manufactured heat spreader
ABS	Acrylonitrile butadiene styrene
°C	Degrees Celsius
CFD	Computational fluid dynamics
CM	Common mode
dB	Decibel
EMI	Electromagnetic interference
GPM	Gallons per minute
Hz	Hertz
Psi	Pounds per square inch
W	Watts
WBG	Wide band gap

GREEK SYMBOLS

μ	Micro

4.1 INTRODUCTION

4.1.1 POWER ELECTRONICS THERMAL MANAGEMENT

State of the art power inverters generate intense heat loads through electrical losses, based on recent trends in power densification in WBG modules. Moreover, the current and switching conditions in these systems can produce extreme EMI levels, which can be amplified by inductive coupling with the metallic cooling solutions intended to ameliorate the heat loads. These adverse conditions may cause premature device failure modes such as wirebond lift-off and substrate

cracking from circuit overloads or thermal runaway if improperly managed, or may contribute to a host of reliability challenges. Additionally, thermal coupling of devices in power modules in the context of traditional cooling schemes will produce non-uniform temperature profiles among devices leading to imbalances in resistance and lifetimes among circuit elements. Conventional cold plates and heat sinks, while great at thermal management through conduction, lack in the ability to eliminate temperature gradients based on their thermal resistances, particularly at interfaces. Additionally, gradients in the cold plates themselves cause the "downstream" regions of the cold plate regions to receive sub-par cooling as a result of increased fluid temperatures, as illustrated in Figure 1. These areas of non-uniform cooling have the ability to cause pre-mature device failure in the hottest regions due to temperature driven reliability failure mechanisms. Consequently, a heat spreader design that can eliminate sharp temperature gradients while providing adequate system cooling would be desirable.

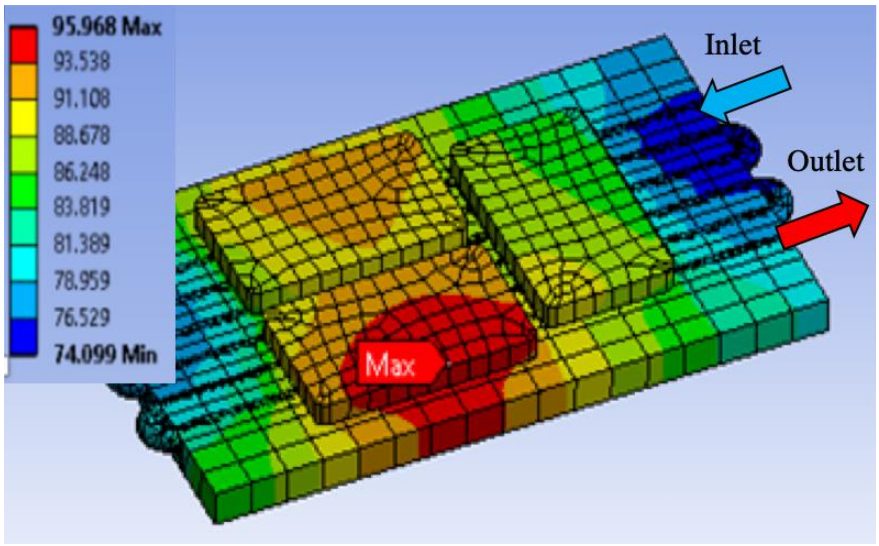

Figure 1: Non-uniform power module cooling with typical cold plate thermal management.

Consistently with their job of heat conduction, cold plates and heat sinks perform the bulk of their cooling through high-conductivity materials, such as aluminum and copper. However, these materials have the added risk of damaging EMI from resonant induced currents in their

electrically conductive construction. Therefore, there is a need for a non-metallic thermal management scheme that can alleviate the electronic coupling while maintaining safe module temperatures. Additionally, non-metallic materials not only have the advantage of low EMI effects, but polymers offer lower density in general, leading to lighter weight in thermal management for mobile and mass-conscious systems.

While cold plates and heat sinks are the common choice of thermal management, there are other active cooling options such as microchannels and spray cooling. Tuckerman et al. demonstrated microchannel cooling in planar circuits with heat flux values approaching 800 W/cm2 [1]. And Hirshfeld et al. also implemented microchannel cooling and was able to reach 1400 W/cm2 [2]. While microchannels are becoming more popular for high heat flux thermal management, the small internal features drive up the pumping cost in the form of pressure drops. Therefore, this type of cooling may only be suitable for applications that have allowance for high pumping system costs.

Spray cooling is another viable option for electronics cooling. who have implemented this technology have obtained heat flux performance values up to 1200 W/cm2 [3]. However, through the process of applying small droplets of coolant onto a heated surface, the small feature sizes required for such process are susceptible to malfunction through clogging. And once more, the pressure drops required to “atomize” the liquid can come at a steep price [1].

4.1.2 JET IMPINGEMENT FOR HOT SPOT CONTROL

As power devices become more powerful, hot spot mitigation is becoming more necessary for the successful prediction of device longevity. As of late, directed jet impingement has traditionally been used in applications such as the increased cooling of turbine blades. In such scenarios, Jambunathan, et al. found that the heat transfer coefficient of directed cooling correlates

with the Reynold's and Prandtl numbers, [4]. With regards to the geometry associated with direct impingement, the spacing between the nozzle exits and base plate display a relationship where increased spacing decreases the rate of heat transfer in particular situations, Huber and Viskanta [5]. In addition to the Reynold's and Prandtl numbers directly relating to the rates of jet impingement heat transfer, it was found that the Reynold's number is further related to the Nusselt number. San et al. [6] showed this relationship to be correlated by a power of 0.6375 with a maximum jet diameter of 6 millimeters. Therefore, this fundamental knowledge can motivate design philosophies for nozzle arrays and how they might interact with the electronic packaging. For example, by holding this relationship to be true, one can properly make a first-pass thermal management design based on the required electrical losses needing to be removed through heat flux.

While these prior works add much to the fundamental understanding of jet impingement technology, power electronics cooling applications have not seen significant adoption. Recently, Wei et al. demonstrated non-metallic hot spot cooling in a chip-scale electronic packaging assembly using nozzle arrays [7]. Using this approach, single or multiple jets, manufactured through ceramic micromachining, can control hot spots in the electronic devices through directed impingement at the critical locations, to affect increased local heat transfer and mitigate lateral spreading of thermal energy.

Additive manufacturing (AM) technologies have recently gained much attention for potential cooling applications, but most approaches have evaluated the use of metallic (thermally conductive) structures using conventional approaches to heat sinks and other cooling techniques for electronics cooling. [8-10]. Yet, polymer AM has matured greatly in recent years, and can offer a unique potential solution to the three-fold problem of EMI, mass and enabling enhanced local

heat transfer with impinging jets. Using 3-dimensional design space to create a jet impingement manifold for directing coolant onto device hotspots provides the opportunity to customize thermal management based on module design and even power dissipation schemes. Recently, Whitt et al introduced a fused deposition molding prototype of an AM heat spreading technology utilizing impingement for cooling in a power module, based on widely available ABS filament methods [11-12]. Yet, even with maturity in the AM process, creating channels for flow of coolant is not without drawbacks, where various printing methods may create unwanted surface roughness and porosity that is deleterious to flow performance.

4.1.3 OBJECTIVE

The manufacturing work presented here is focused on providing a clear pathway to utilize additive manufacturing and post-print processing to reduce the negative impacts of surface roughness and ensuring optimal flow performance. A few process flows are presented here, with a discussion of the implications to pressure drop and heat removal performance stemming from the manufacturing method. In addition to evaluating manufacturing finishing process honing, CFD is also used to examine predicted performance of the additive manufactured heat spreader (AMHS) with respect to power module cooling capacity. The resulting heat spreading device is optimized to reduce EMI noise, while maintaining sufficient cooling capability at a low weight.

4.2 MATERIALS AND METHODS

4.2.1 ADDITIVELY MANUFACTURED HEAT SPREADER DESIGN

Figure 2.a presents the additive manufactured heat spreading device, Figure 2.b gives an isometric view of the heat spreader and 2.c is a 2D cross-section showing the fluid paths designed for direct impingement supplied by a manifold delivery network. This device is designed to integrate directly with a novel high-powered inverter. However, the working principles and design

considerations can be expanded to numerous potential applications. For this generation design, the localized cooling is designed for integration with wide band gap power modules for use in power electronic devices. More specifically, the power modules being cooled are for use in a T-type inverter for applications in hybrid-electric propulsion systems.

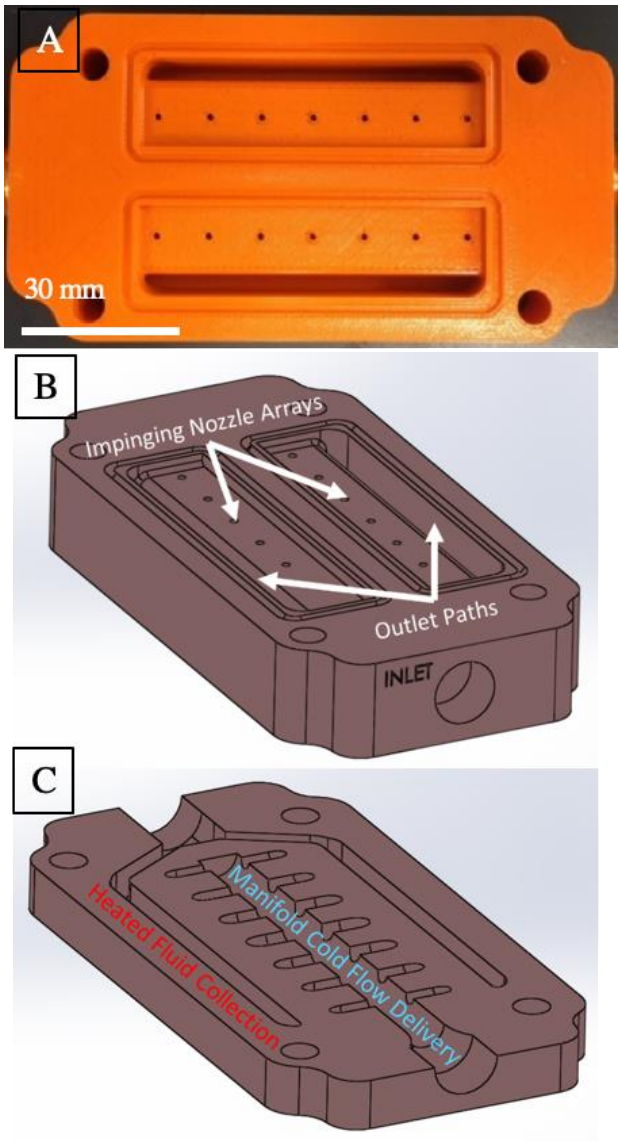

Figure 2: a) Direct printed ABS AMHS device. B) AMHS isometric view with nozzle callouts. C) AMHS cut view showing internal device features

The nozzles illustrated are placed such that the cold working fluid impinges directly onto the module's hot spots, corresponding to the wide bandgap switch locations. Before impingement,

the fluid is first routed to through a low pressure drop manifold. This manifold can not only be optimized with respect to pressure drop, but also such that the module is uniformly cooled through increased flow in critical areas of higher importance. In this case the nozzle diameters were varied slightly to create uniform exit velocities at each of the 14 impingement sites, based on pressure variations in the manifold, as determined by a preliminary CFD analysis.

After impingement, the fluid is forced to flow in strategically placed outlets such that the warm fluid "spreads" the thermal energy to produce uniform temperature contours instead of sharp, non-uniform module temperature gradients. In this design, two outlet paths are placed laterally next to each row on impingement nozzles, which then re-combine to form a single flow outlet. While the re-combination has the chance to increase the pressure drop seen in the device, having a single outlet greatly reduces testing and integration complexity.

4.2.2 ADDITIVE MANUFACTURING PROCESS

Since this design is based on the use of internal 3D geometries to enable a nozzle manifold for multi-site impingement cooling, additive manufacturing methods naturally offer a pathway to manifold construction. The ability to customize flow paths and allow for highly configurable geometries gives designers a high degree of flexibility in flow optimization for heat transfer performance; however, most readily available printing technologies are not necessarily "plug and play" for generating flow paths. Using fused deposition molding (FDM) AM offers a well-established method of quick production, reasonable tolerances, with customizable and immediate implementation. However, if the component is used for fluid applications, new challenges such permeability and surface roughness arise. As the deposited layers fuse together, traces of the individual layers may still be visible. As such, the surfaces may exhibit large surface roughness on the order of the FDM extruder nozzle size. Moreover, often times these layers are not completely

fused together. While each layer may be solid, the combined solid may let fluid/coolant pass through, particularly when under pressure. To counteract these issues, this effort utilized chemical vapor smoothing and external coating to seal and smooth the part. Figure 3.a shows the before and after of an acrylonitrile butadiene styrene (ABS) plastic 3D printed surface treated with acetone vapor.

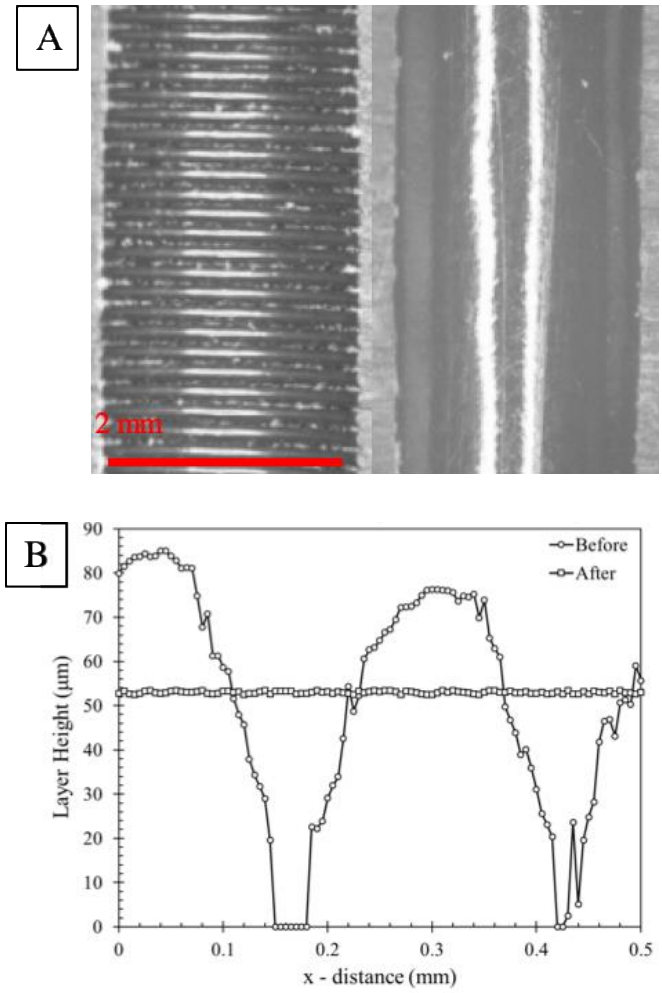

Figure 3: A) FDM ABS plastic before (left) and after (right) treated with chemical vapor smoothing. B) surface profiles of 3D printed ABS plastic before and after acetone vapor treatments.

As seen, the treated surface is considerably smoother, and has been shown to also be resistant to permeation, contrary to the “untreated” surface. To quantify just how much smoothing

is occurring with the acetone vapor, surface profiles of the samples were obtained using an optical profilometer. As Figure 3.b shows, before smoothing the individual plastic layers are visible with an average peak-to-trough height of approximately 80 microns. However, after smoothing, that value drops into the nano-meter scale. One aspect to be noted with the acetone smoothing method is that with ABS plastic, the acetone does not dissolve material. Instead, it provides local surface dissolution and re-deposition of material into the troughs. This explains that while the average roughness height after smoothing is under 1 micron, although the channel geometry (i.e. hydraulic diameter) compared to pre-processing is not significantly changed when treated for small times.

4.3 RESULTS AND DISCUSSION

4.3.1 MANUFACTURING AND SURFACE OPTIMIZATION FOR FLOW

When considering the post-print fabrication of chemical vapor smoothing for hermeticity and control of surface roughness, the printing method's inherent problem of generating large pumping costs in the form of pressure drop can be reduced. With large surface roughness values, pressure drops may increase across the part and cause the performance cost to also increase. Therefore, if chemical vapor smoothing is to be the chosen smoothing process, then individual parameters surrounding it need to be optimized. Keeping the vapor pressure of the acetone constant, preliminary studies show that an increase in processing time can lower pressure drop values across test specimens, Figure 4.

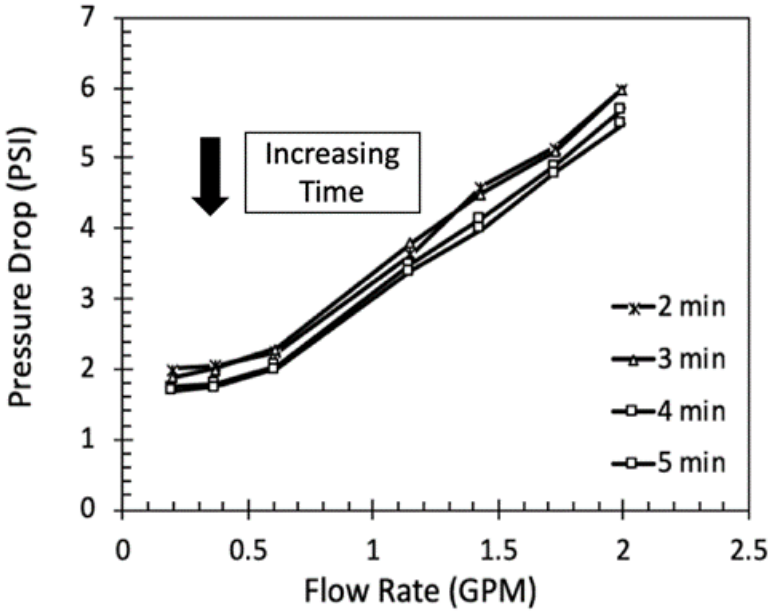

Figure 4: Pressure drop reduction with increasing time of chemical vapor smoothing

4.3.2 CFD EVALUATION AND PERFORMANCE PREDICTIONS

Having developed a method for fabrication of an internal flow manifold for impingement hot spot management, CFD simulations were utilized to predict the cooling performance relevant to a T-type inverter assembly with 3 SiC high voltage power modules generating heat while attached to a base plate. As a benchmarking exercise, a standard cold plate cooling configuration was compared with three of the AM heat spreader devices with regard to thermal performance as measured by the base plate temperatures near the device locations. These modules contain 14 smaller die locations where the heat is actually generated. The total heat load was assumed to be divided evenly among each die location. This simulates real electrical platforms in which inverter devices carry different switching loads and produce electrical and thermal losses. Figures 5.a and 5.b display preliminary results when cooling a single module with a conventional cold plate and the impinging hot spot controlling AM design, respectively.

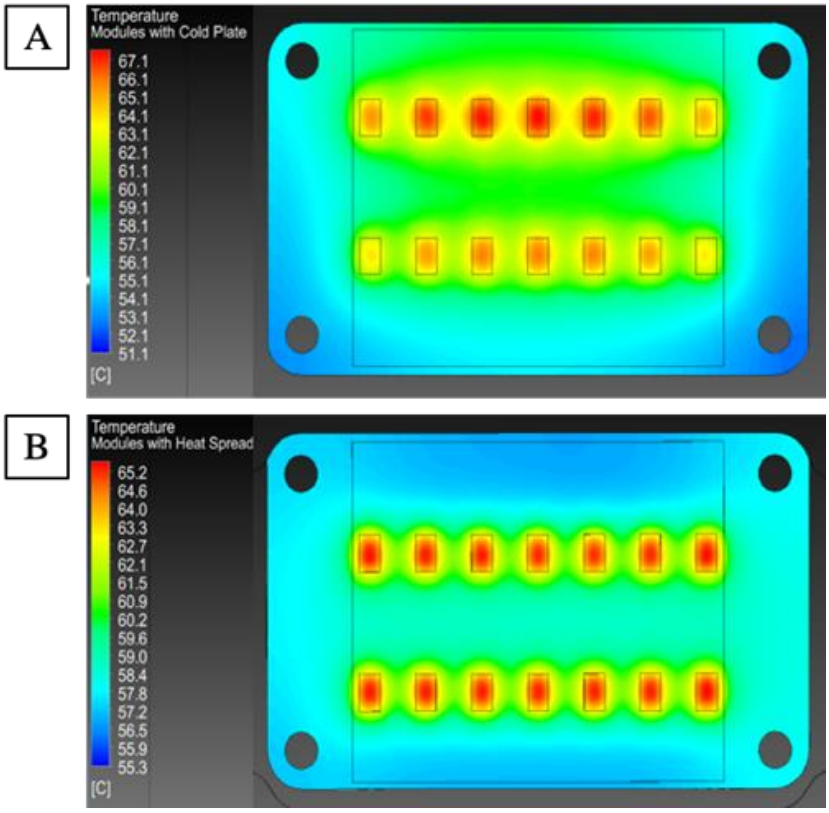

Figure 5: A) Temperature contours in a single module cooled by a conventional cold plate. B) Temperature contours in a single module cooled by the new local impingement device

As displayed, Figure 5.a shows a power module with non-uniform temperatures across device locations in the form of elliptical temperature contours, which arise from the conduction driven mechanism of a typical cold plate thermal solution. While working fluid in the cold plate convectively extracts energy from the module, the heat transfer is ultimately conduction limited at the module to cold plate interface. Moreover, as the fluid absorbs energy from the intense heat loads, spatially downstream portions of the module(s) experience less heat removal due to an effectively higher cold plate "free stream" temperature. The net result is temperature imbalances among devices in the module, with co-heating effects in the center of multiple device arrays, and furthermore each device is significantly hotter than the surrounding baseplate. On the contrary, the new localized, impingement-based heat removal device focuses its cooling activity at the hot spots, and convectively removes the heat into the working fluid, rather than relying on conduction

mechanisms in the rest of the baseplate where no heat loads exist. Effectually, high local heat transfer coefficients can greatly reduce heat spreading in the module, and eliminate the effects of device co-heating. Figure 5.b gives the resulting temperature contours with the new AM cooling device. The impingement mode thermal contours now display better temperature uniformity along the length of the power module with no visible signs of co-heating. Thus, equilibrated temperatures at the devices can be achieved, and the cooling localization has the benefit of decreasing maximum hot spot temperatures up to 2°C for similar flowrate considerations predicted by this CFD evaluation.

4.3.3 EXPERIMENTAL HEAT TRANSFER PERFORMANCE

To validate the simulated results obtained with the power module assembly, a heating block apparatus, Figure 6.a, was developed to experimentally evaluate the thermal management of the power module. A block of aluminum was machined to house two resistive cartridge heaters, Figure 6.b. By tightly packing insulation around block, the generated power was "channeled" through 14 individual milled "extrusions" to replicate the creation of hot spots by WBG devices in a power module, upon which the thermal management device can be attached. Moreover, two thermocouples were placed in each extrusion in the direction of heat flow through the material. Thus, by knowing the temperature at each point, $T_t - T_b$, the distance between the two, d, and the cross-sectional area of the extrusion, A_c, one can determine the power flux through each extrusion according to Equation 1.

$$P_{heater} = kA_c \frac{(T_t - T_b)}{d} \quad (1)$$

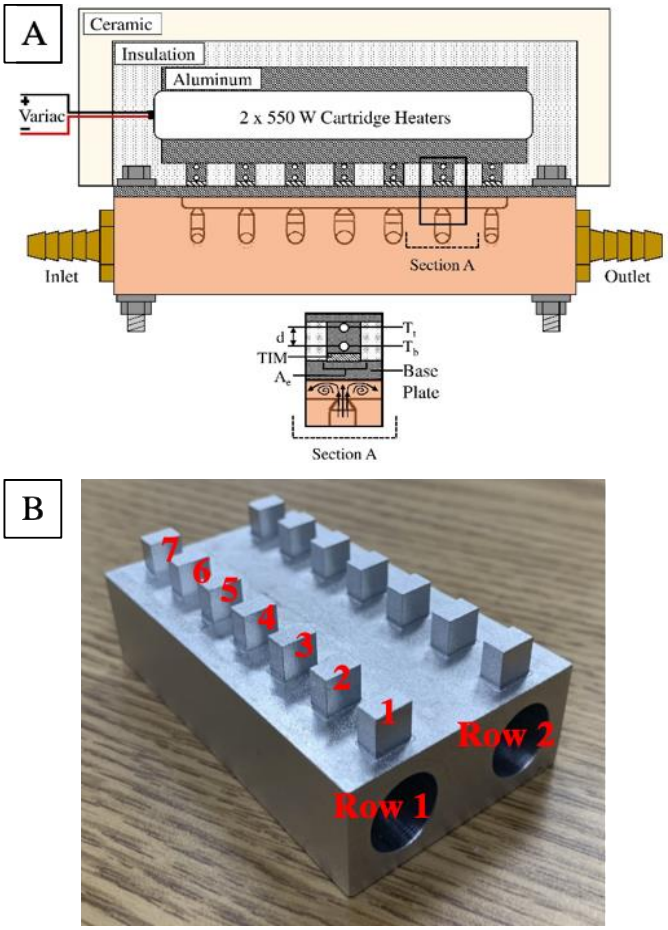

Figure 6: A) Heating block apparatus with the AMHS attached for directed cooling. B) Aluminum heating block with extrusion nomenclature

Furthermore, a custom flow loop was built to provide the liquid cooling to the system and monitor key metrics such as pressure drop and temperature difference across the cooling device and volumetric flow rate. Therefore, the enthalpy rise of the fluid as it cools the heated test section can also be determined according to Equation 2.

$$P_{fluid} = \dot{m} C_p (T_{outlet} - T_{inlet}) \quad (2)$$

Here $\dot{m}$ is the mass flow rate of the fluid and $T_{outlet} - T_{inlet}$ is fluid temperature rise measured across the thermal management device. By measuring both the change in fluid enthalpy and conducted power in the heating block extrusions, a comparison can be made to provide a metric of experimental precision to confirm the results are accurate.

Lastly, the effective thermal resistance between the coolant and the heating block can be determined using Equation 3, where $T_{heater,ave}$ is the average temperature of the heating block extrusions and $T_{fluid,ave}$ is the average of the inlet and outlet temperatures. This effective thermal resistance can be a useful comparison between cooling method performances. In this study, the thermal management performance of the AMHS device is compared against a 4-pass, Lytron Hi-Contact Tube Liquid Cold Plate for benchmarking purposes, as well as the CFD simulation results.

$$R_{th} = \frac{(T_{heater,ave} - T_{fluid,ave})}{P_{fluid}} \tag{3}$$

$$T_{fluid,ave} = \frac{(T_{outlet} - T_{inlet})}{2} \tag{4}$$

$$T_{heater,ave} = \frac{\sum_{i=1}^{14} T_{b,i}}{14} \tag{5}$$

Heating profile comparisons were measured for a distributed heat source using 2 150 W strip heaters as well as the hot spot emulating heating block. In the strip heater arrangement, the resulting heating profile was non-uniform, but provides an alternative evaluation of cooling performance between a standard cold plate and the AM impinging design. Figure 10 gives a comparison of the temperature profiles created by each experimental setup. These profiles were gathered using IR imaging with a black rubber coating applied to the aluminum surface to provide high quality imaging. Additionally, no active cooling was utilized so that the parabolic heating profiles as noted in the cold plate simulations could still present. As seen, two rows of line measurements are taken on each setup. This serves the purpose of outlining the temperatures where each row of nozzles in the AMHS device will impinge upon. Figures 7a and 7b give the thermal

images of the strip heater and heating block setups, respectively. Figure 7c displays the results of the line measurements.

As indicated by the IR thermography results, the heating block has a centered, parabolic profile and displays clear regions where the effects of the heater extrusions can be seen. In the experiment, both heaters were applied with 300 W, upon which the data shown was collected once the peak temperature reached approximately 65 °C. For both setups, it was at this temperature that the "hot spots" could most clearly be visualized due to heater power ramp rate and rate of conduction in the aluminum.

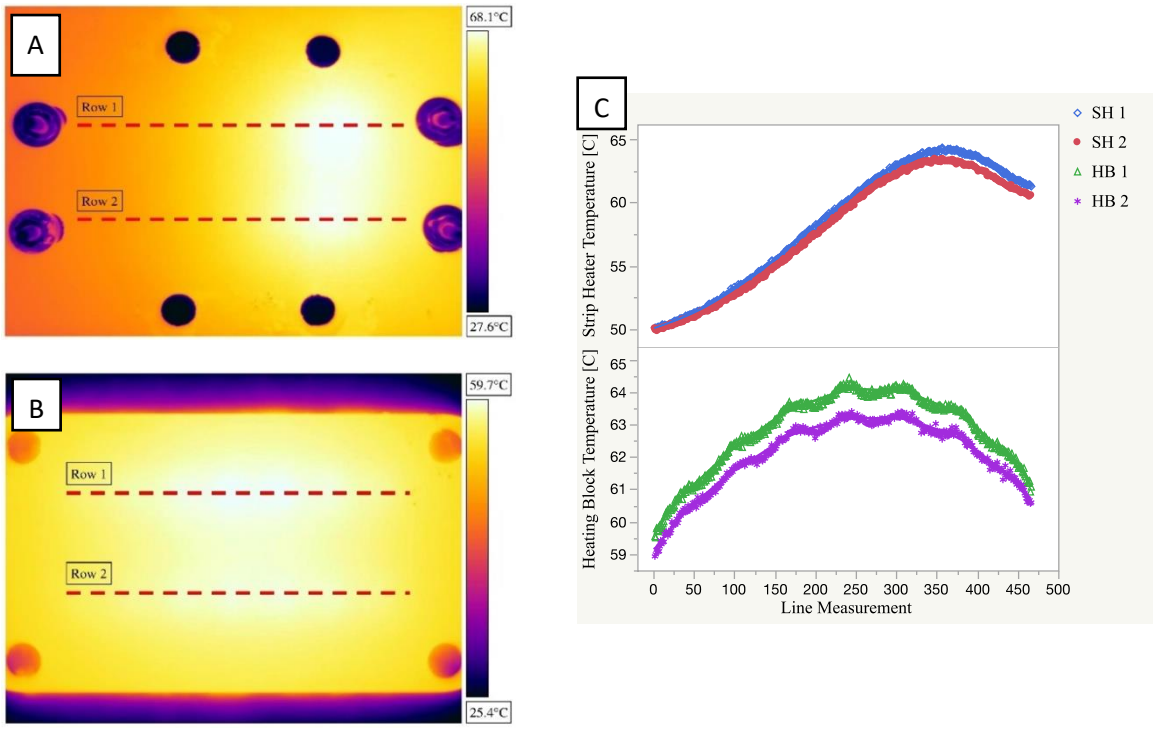

Figure 7: A) Strip heater (SH) assembly thermal image. B) Heating block (HB) assembly thermal image. C) Thermal setup temperature profile comparison.

To characterize the flow and heat transfer performance, a flow loop test bed was constructed, and the inlet water coolant temperature was maintained at 20°C, with flow rates varying from 0.2 – 2.3 GPM. Figure 8.a presents the thermal resistance between the coolant and

heated base plate across varying power inputs in the strip heater experimental setup. With an input power ranging from 100 W – 250 W, the results show a consistent thermal performance, as the equivalent resistance flattening out at the 2 GPM point. Additionally, there is an approximately 0.6 K/W resistance difference in the 200 W test of both cooling schemes. Using this value, the equivalent heat transfer coefficient over the entire cooling area can be calculated, Figure 8.b. Again, the heat transfer coefficient slope gradually declines as the equivalent flow rate from Reynold's number approaches 2 GPM, with a max value of 4000 W/m^2K.

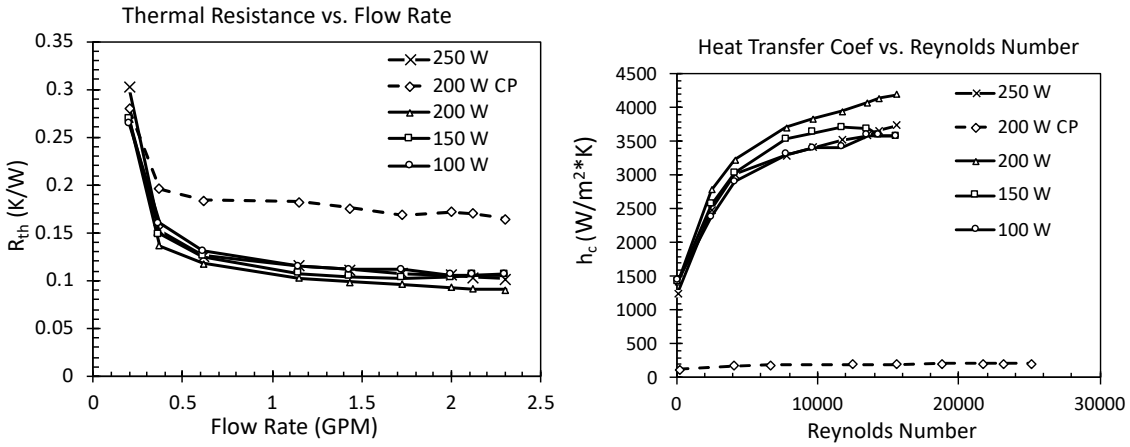

Figure 8: A) AMHS thermal resistance on varying power loads compared to the cold plate (CP). B) AMHS heat transfer coefficient performance.

Having demonstrated improved heat transfer performance even on a distributed heat load, further testing with hot spot creation via the emulated power module heater block was performed. For this set of tests, a total input power of 300 W was applied to the two cartridge heaters with the flow loop coolant set at 20°C varying from 0.2 – 2.1 GPM. In addition to comparing the jet impingement performance against the cold plate, the experimental results were compared to the CFD simulation for validating trends. Similar to the prior results with the strip heaters (distributed heat load), Figure 9.a gives the resulting equivalent thermal resistance of the two experimental tests as compared to the CFD study. As seen, there is a consistent 0.5 – 0.7 K/W difference in

resistance between the cold plate and AMHS device, with slight variations above the 1.5 GPM mark. Moreover, the AMHS resistance curves matches the trend of the simulated performance well, showing that the heating block is suitable for mimicking power module hot spots. One point of explanation for the difference in resistance could be the lack of an interfacial thermal interface layer in the CFD model at the heater block-base plate interface. Therefore, it could be inferred that this interface resistance is approximately 0.5K/W.

Secondly, Figure 9.b gives the temperature of the extrusions for each cooling scheme, where the values are the average of the 14 extrusions, $T_{heater,ave}$. As expected from the thermal resistance results, there is a considerable difference in average device temperature of 20 – 25°C between the cold plate and AMHS device. And once more, the trend of the data set matches that of the simulated results, with the discrepancy coming from the difference in equivalent thermal resistance of the system.

In addition to the targeted hot spot capability to lower device temperatures, the jet impingement zones are also used to create more uniform temperatures across the power module. Due to reliability issues such as current imbalances and device failure resulting from unbalanced thermal loads, it is critical that the thermal management system have this balancing capability. Figure 10 is shown to present the increased balancing functionality of the AMHS device against the standard cold plate at a flow rate of 2.0 GPM. Each cooling method shows two temperature profiles, each representing one row of seven aluminum extrusions. For proper thermal management, we would expect to see uniform temperatures across the seven hot spots in the same row, and ideally the same temperatures across the two rows to prevent current imbalances and reduced reliability. In other words, all 14 extrusions should see relatively the same temperature. As seen, the extrusions under the cold plate regime do not show consistent temperatures in the two

rows. Along the rows, there is an approximately 20 - 30°C temperature difference between locations one and seven. And furthermore, there is a consistent 10 - 20°C variation across the two rows of extrusions.

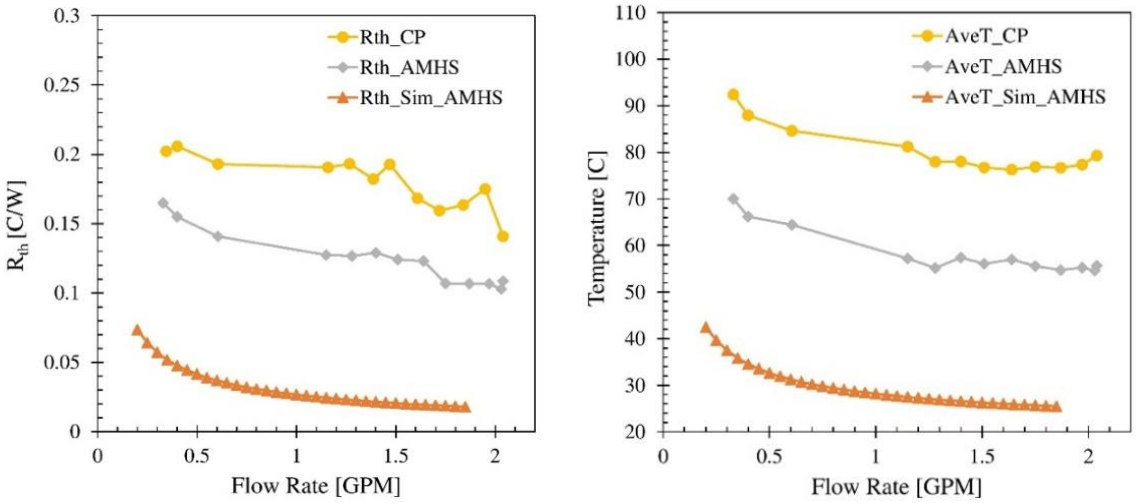

Figure 9: A) Thermal resistance comparison between the AMHS, cold plate (CP) and simulated AMHS (Sim_AMHS). B) Average extrusion temperature for each cooling scheme.

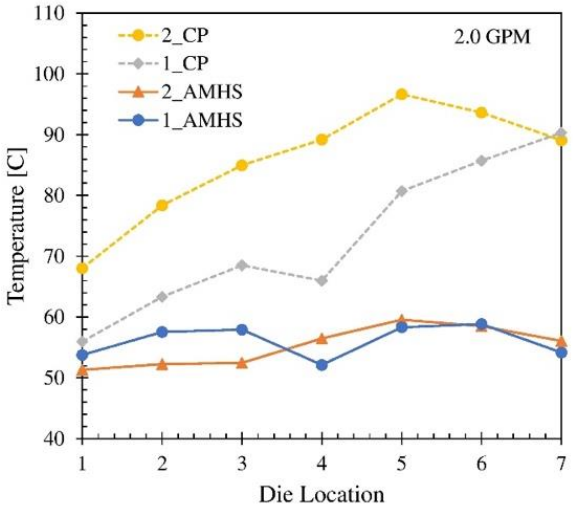

Figure 10: Extrusion temperatures at 2.0 GPM for each row (1 and 2) displaying large differences with cold plate cooling and minimal with the AMHS cooling scheme.

To further illustrate the level of improvement in thermal balancing with the AMHS device, two visual depictions are presented in Figure 11. In Figures 11a and 11b, top-view drawings are shown with each extrusion location colored to represent its temperature at 2.0 GPM to visualize

the thermal gradients with the cold plate and AMHS, respectively. In Figure 11a, large color variations can be identified along the direction of the coolant in the cold plate. However, in Figure 11b, this variation is minimized with the localized cooling through jet impingement.

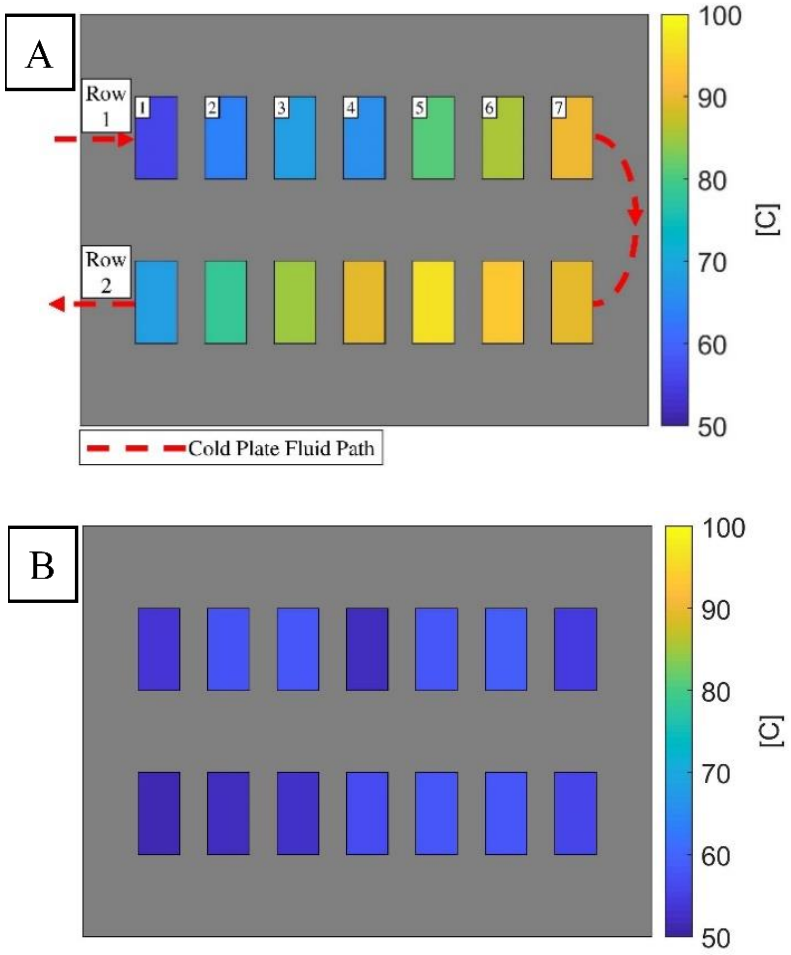

Figure 11: Temperature profile of the heating block during thermal management by the A) cold plate and B) AMHS device.

4.3.4 EMI EFFECTS TESTING

In addition to being lightweight, polymeric materials also dampen EMI noise levels in power-electronics as compared to metallic parts through the reduction of parasitic capacitance. To evaluate the EMI noise reduction capacity of the heat spreader, simulations were performed in the presence of a high-powered inverter. At the time of switching operation in the converter, the EMI

become one of the major issues to look at. Common mode EMI depends on dv/dt stress across parasitic capacitance. A half bridge module has been taken into consideration for case study. The major parasitic capacitance which is influencing CM EMI is the capacitance between drain of the MOSFET to the power ground. A parametric study has been done with FEM simulation tool (ANSYS Q3D) to extract parasitic capacitance matrix. As stated, the CM noise has a proportional relation with the magnitude of parasitic capacitance. In Figure 12 we can see an attenuation of 60 dB has been achieved after replacing conventional metallic heatsink with the proposed one. Furthermore, additional results of EMI simulations that show a reduction on the order of 1000 in the equivalent capacitance of the heat spreader design with a polymer material. Combined, the common mode noise and capacitance represent a large reduction of harmful EMI effects when using a non-metallic material with a high-powered half-bridge module.

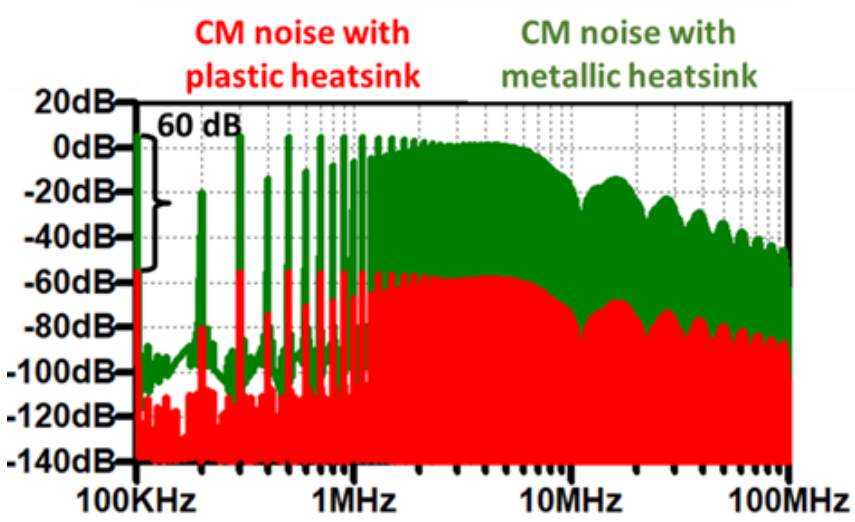

Figure 12: Common mode noise simulations showing a 60 dB reduction in EMI noise with a polymer heat spreader.

4.4 CONCLUSION

With the increasing density of power-electronics, hot-spot mitigation must become a top priority to ensure reliable devices, and cleverly thermal engineered systems may provide the most

direct pathway to enabling next generation, high power dense power electronics. Directed cooling using high heat transfer coefficient approaches can offer customized solutions for managing hot spots, and additive technology represents one potential solution toward this goal. In this work, an additively manufactured, non-metallic heat spreader with direct cooling has been demonstrated here to have the improved cooling performance over conventional metallic cold plates, and particularly with regard to improved hot spot temperature management. Moreover, its polymer construction helps in reducing system weight and damaging EMI effects. Using commonly available 3D printed materials and processing, the surface roughness and sealing properties of the part were fine-tuned to produce optimal surface characteristics. Furthermore, despite the promising results already demonstrated, even greater heat removal may be obtained by using CFD for performance optimization, design features such as nozzle and manifold geometries can be selected to produce the highest heat transfer rates with the lowest impingement-plate temperature gradients. Additionally, further development in optimal materials selection for EMI damping may further reduce harmful parasitic capacitance and EMI noise levels. With this reduction, EMI filter size and weight may be able to be reduced, further benefiting the effective system power density.

4.5 ACKNOWLEDGEMENTS

The authors would like to thank the POETS ERC for funding this work, which is based upon work supported by the National Science Foundation under Grant No. 2014-00555-04. Furthermore, special thanks to Skyler Hudson, Bakhtiyar Nafis, Balaji Narayanasamy, and Amol Deshpande for their assistance in various components of this study. Any opinions, finding, and conclusions or recommendations expressed in this material are those of the author(s) and do not necessarily reflect the views of the National Science Foundation.

4.6 REFERENCES

[1] D. Sharar, N. Jankowski and B. Morgan, Review of Two-phase Electronics Cooling for Army Vehicle Applications, 2010.

[2] H. Hirshfeld, I. Silverman, A. Arenshtam, D. Kijel and A. Nagler, "High heat flux cooling of accelerator targets with micro-channels," Nuclear Instruments & Methods in Physics Research Section a-Accelerators Spectrometers Detectors and Associated Equipment, vol. 562, no. 2, pp.903-905, Jun 2006.

[3] M.R. Pais, L.C. Chow and E.T. Mahefkey, "Surface roughness and its effects on the heat transfer mechanism in spray cooling," Journal of Heat Transfer, vol. 114, no. 1, pp. 211-219 1992.

[4] Jambunathan, K., Lai, E., Moss, M. A., & Button, B. L. (1992). A review of heat transfer data for single circular jet impingement. International journal of heat and fluid flow, 13(2), 106-115.

[5] Huber, A. M., & Viskanta, R. (1994). Effect of jet-jet spacing on convective heat transfer to confined, impinging arrays of axisymmetric air jets. International Journal of Heat and Mass Transfer, 37(18), 2859-2869.

[6] San, J. Y., Huang, C. H., & Shu, M. H. (1997). Impingement cooling of a confined circular air jet. International journal of heat and mass transfer, 40(6), 1355-1364.

[7] T. Wei, H. Oprins, V. Cherman, J. Qian, I.D. Wolf, E. Beyne and M. Baelmans, "High-efficiency polymer-based direct multi-jet impingement cooling solution for high-power devices," IEEE Transactions on Power Electronics, vol. 34, no. 7, pp. 6601-6612 2019.

[8] P. Dupuis, Y. Cormier, M. Fenech, and B. Jodoin, “Heat transfer and flow structure characterization for pin fins produced by cold spray additive manufacturing,” Int. J. Heat Mass Transf., vol. 98, pp. 650–661, 2016.

[9] Dede, E. M., Joshi, S. N., and Zhou, F., 2015, “Topology Optimization, Additive Layer Manufacturing, and Experimental Testing of an Air-Cooled Heat Sink,” J. Mech. Des., 137(11), p. 111403

[10] Wong, M., Owen, I., & Sutcliffe, C. J. (2009). Pressure loss and heat transfer through heat sinks produced by selective laser melting. Heat Transfer Engineering, 30(13), 1068-1076.

[11] R. Whitt et al., "Heat Transfer and Pressure Drop Performance of Additively Manufactured Polymer Heat Spreaders for Low-Weight Directed Cooling Integration in Power Electronics," 2019 18th IEEE Intersociety Conference on Thermal and Thermomechanical Phenomena in Electronic Systems (ITherm), Las Vegas, NV, USA, 2019, pp. 451-455.

[12] Reece Whitt and David Huitink. Thermal Validations Of Additive Manufactured Non-Metallic Heat Spreading Device For Hot Spot Mitigation In Power Modules. International Symposium on Microelectronics Fall 2019, Vol. 2019, No. 1, pp. 000398-000403.

5. THERMAL MANAGEMENT OF A 150KW SIC MOSFET BASED INVERTER WITH NONMETALLIC ADDITIVELY MANUFACTURED JET IMPINGEMENT COOLERS

Co-Authors: Zhao Yuan, Fang Luo, and David Huitink

ABSTRACT

Power electronics switching devices utilized in traction, propulsion and power generation applications require advanced thermal management systems and extensive electromagnetic interference filtering components. Traditional indirect cooling methods exhibit limited ability to target switching location hot spots, causing current imbalances due to thermal gradients. Additionally, they rely on metallic structures directly integrated with module base plates, allowing for an accentuation of common mode noise. These effects present themselves concurrently, creating reliability concerns while requiring further noise filtering. This work demonstrates the integration of a nonmetallic jet impingement cooler for direct base plate thermal management of a 150kW SiC inverter. The use of nonmetallic structures manufactured through additive techniques limits low-induction capacitance pathways by 99%, leading to a 25dB reduction in common mode noise. Impingement jets focused on module hotspots reduces maximum device temperatures and increases thermal uniformity. Finally, by attaching individual jet coolers to each power module, hydraulic circuit networks are used to demonstrate thermal balancing between power devices for optimal current sharing.

5.1 INTRODUCTION

5.1.1 ADVANCED COOLING OF POWER ELECTRONICS

High-voltage power electronics devices designed for more electric aircraft (MEA), electric vehicles and power generation require high switching frequencies in the kHz - MHz range. Alternating current devices, such as traction motors, deliver useful work at higher efficiencies if the supplied power is generated with minimal switching losses [1]. As a result, Silicon-Carbide

(SiC) and Gallium-nitride (GaN) MOSFETS operating at high frequencies generate intense heat loads that, if not properly managed, can cause premature device failure. The most common failure modes of power electronics devices include wirebond cracking, solder joint fatigue and delamination of the substrate layer [2]. From a physics of failure perspective, the underlying mechanism driving device malfunction is thermal cycling [3]. Due to mismatches in coefficient of thermal expansion (CTE) between power module layers, nonuniform stresses and loading conditions are exerted onto critical electrical components [4]. Overtime, this cyclic behavior created by necessary systematic power profiles causes permanent damage that exceeds allowable fatigue life predictions. Techniques designed to reduce the stresses experienced by interconnects have been proposed, including transient liquid phase die-attach bonding [5] and low CTE substrates [6]. While these methods can increase the upper device temperature limit by 50-100 °C [7], the interaction between the switching devices and the thermal management system remains a critical task to be optimized in parallel with reliability efforts.

Modern power electronics modules, including options by CREE, Infineon and Semikron are designed with a thermally conductive base plate for removal of thermal energy. When integrated into electric vehicle and hybrid-electric aircraft systems, the switching devices are typically cooled using cold plate technology. This method requires a thermal interface material (TIM) between the base plate and cold plate, resulting in a major thermal bottleneck. Moreno et. al. shows that on average, packaging components (substrates, base plates, and TIMs) can account for up to 85% of total junction-to-fluid thermal resistance [8]. Therefore, the removal of the TIM layer can single handedly improve device reliability.

To remove this TIM layer, the cooling medium must come into direct contact with the power module base plate. Microchannel coolers are a popular option to replace bulk-convective

cold plates as the presence of micro-sized features attached to module base plates can reduce thermal resistance values by 50% [9]. This type of device is well suited for small electrical footprints as the pressure drop resulting from a high-density number of features produces immense fluid friction losses. Therefore, unless a microchannel cooler can be sufficiently integrated into the direct bonded copper layer of the power module, it is likely that the resulting pressure drop would be greater than allowable thresholds with respect to cooling efficiency [10].

A second approach to direct thermal management is spray cooling. By impinging atomized coolant onto a targeted hot spot, a constant stream of boiling droplets can achieve heat fluxes as great as 1000 W/cm^2 [11]. For a typical IGBT module, this heat flux is more than sufficient. However, concerns with nozzle clogging, critical heat flux regimes and insufficient thermal energy to promote two-phase heat transfer restrict the usefulness of this technology for power electronics [12].

While each of these two approaches have potential to create uniform temperatures throughout a power electronics system, they are largely limited by their pressure drop requirements given the small hydraulic diameter of physical features. One method that combines the effectiveness of single-phase spray cooling with direct fluid contact in microchannels is the jet impingement method. The efficiency of this method lies in the ability to target individual power module hot spots without the concerns of reaching the critical heat flux values and the co-heating of electrical devices through microchannel base plates. Heat flux values up to 250 W/cm^2 have been reported using single-phase impingement schemes [13]. While not as effective as spray cooling, the pressure drop required by jet impingement devices can be significantly less and on the order of 70 kPa [14], as opposed to 150 kPa with spray cooling [15].

With respect to power electronics systems, namely high-voltage inverters and converters, there have been a limited number of jet impingement coolers demonstrated on such systems. Gould et al. showed a 120 °C reduction of a SiC device junction temperature using jet impingement compared to a standard off the shelf cold plate and a power load of 151 W [16]. In this study, a metallic impingement block with an array of 200 µm nozzles is attached to a 600V/50A SiC module used for battery conversion. Mouawad et al. proposed a highly integrated impingement cooler with a 10kV/20A SiC module where the thermal management system is designed for impingement cells to target individual hot spots [17]. In this work, the module architecture is directly mounted into the cooler for maximum cooling efficiency, resulting in a thermal resistance of 0.38 K/W.

While a low thermal resistance value is needed for sufficient thermal management, temperature differences between internal module devices can drastically affect reliability. Bhunia et at. integrated a jet impingement cooler onto a single power module with 12 internal IGBTs [18]. They found at a flow rate of 1.75 gpm and a power load of 600 W, the maximum temperature difference between IGBT locations was approximately 1.5 °C. Thus, it has been shown that not only can jet impingement cooling provide lower average junction temperatures than standard cooling methods, but also limit internal temperature variations between switching locations.

In previous works, Whitt et al. have demonstrated the use of a non-metallic impingement cooler for power module integration [19-20]. Using experimental techniques to emulated power module hot spots, effective thermal resistance values of 0.1 K/W were achieved over 14 hot-spot locations. In conjunction with improved thermal management, additive manufacturing techniques were used to construct the cooler out of non-metallic components. EMI shielding experiments with a single module showed a 25 dB reduction in common mode noise. These works showed the

usefulness of the impingement cooler method on the module scale. However, it has yet to be shown how this cooling scheme scales and integrates on the system-scale with several power modules. In this work, the authors investigate the thermal performance of a high-voltage inverter with non-metallic impingement coolers for the purpose of providing cross-module thermal balancing and EMI noise reduction.

5.3 IMPINGEMENT COOLER DESIGN

5.3.1 COOLING PRINCIPLE AND MECHANISMS

The jet impingement cooler designed for this study utilizes round nozzles that are positioned to impinge onto the base plate of a CREE power module where internal SiC devices are located. The nozzles are 1.5 mm in diameter, D, and are a distance, H, of 4.5 mm away from the base plate surface, giving a H/D ratio of 3. It is widely known for submerged jet impingement, and H/D ratio of 2-8 is the optimum value. As described by Zuckerman et al., a ratio less than two creates issues with extreme fountain effects, low turbulence generation and highly constrained flow [21]. For a ratio greater than 8, the nozzle shape and distance between multi-nozzle systems greatly affect the kinetic energy of the fluid as it approaches the target wall. In this study, it was determined that an H/D value closer to two would be ideal as to avoid over-confining the flow and maintain sufficient separation between hot spots required a nozzle pitch of 11 mm. Figure 1a shows an isometric overview of the cooler, with lateral coolant collection paths to separate two rows of power module hot spots. As seen in figure 1b, the cooler directly bolts to the power module using four mounting locations and used two barbed fittings for coolant routing. While not shown here, a liquid gasket material is applied onto the top surface of the cooler, which is then promptly bolted to the module. This provides a water-tight seal, which is a major concern with direct cooling methods. Finally, figure 1c gives a transparent view of the cooler, showing the internal coolant

manifold and subsequent routing to each nozzle with a constant pitch of 11 mm between locations. The volume of the cooler is 138 cm^3 with a footprint of 40 cm^2.

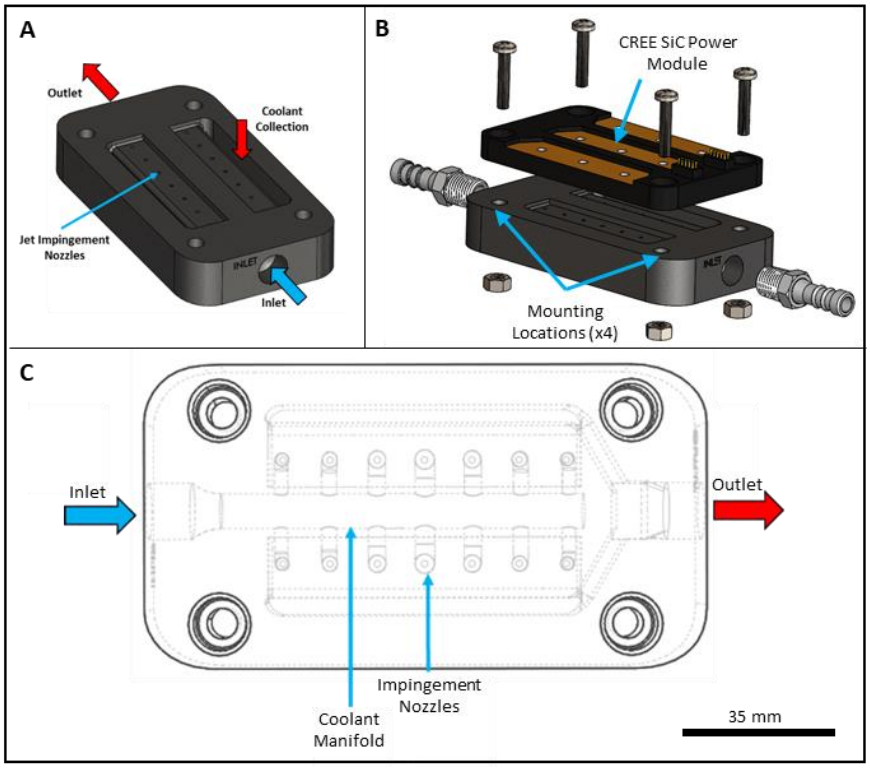

Figure 1: A) isometric view of the impingement cooler. B) method of attaching the cooler to the SiC power module. C) transparent view of the cooler showing internal coolant routing paths.

5.3.1 COOLER MANUFACTURING

To minimize parasitic capacitance pathways throughout the thermal management system when integrated with the power electronics, it was vital to use a non-metallic framework. Popular polymeric manufacturing techniques include investment casting, micromachining, and additive manufacturing. Casting techniques allow for excellent design flexibility but are limited by the melting temperature of the sacrificial material. Common 3D printed casting resins, such as those intended for jewelry and dental products, can have a burnout temperature of over 250 °C. This limits the non-metallic materials that can be formed using this method. Micromachining technique provide a reduce level of design freedom but enable more materials to be utilized. Materials such

as ABS, PLA, Nylon and PMMA can be easily machined into high-temperature stable components. Therefore, it was necessary to choose a compromise between these two methods: using additive techniques to directly print a high-temperature stable non-metallic part. For this, the printed process known as multi-jet fusion was applied. As seen in figure 2, this process is similar to direct metal laser sintering, but instead the base material used is Nylon PA 12. Technical specifications of this material include a water absorption level of 0.5 ± 0.2% at 50% relative humidity and a heat deflection temperature of 175 °C at an ambient pressure of 0.46 MPa. It is important to note that this process can be directly integrated into the cooling system without any post processing. Once the internal powder from the sintering process has been removed and all surfaces are cleaned, the device can be considered complete.

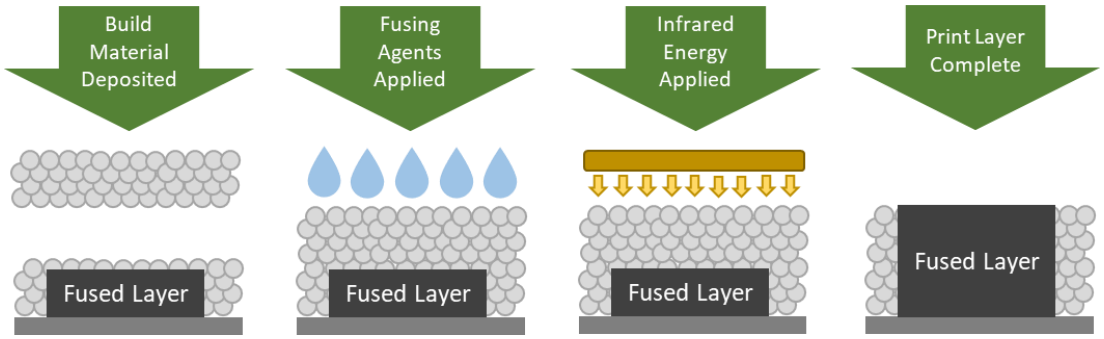

Figure 2: Process overview of the multi-jet fusion printing method for a high-temperature stable, non-metallic construction.

5.4 INTEGRATED ASSEMBLY

5.4.1 INVERTER DESIGN

The electrical device included in this systematic case study is a 450 kVA, three-level T-type neutral point clamp traction inverter utilizing silicon carbide power modules [22]. The T-type architecture provides advantages over other inverter types as electrical inefficiencies and switching

losses are reduced compared to lowered-level arrangements. Figure 3a shows the final assembly of one 150 kW phase of the three-phase inverter, with a standard cold plate attached for thermal management. A more detailed look at the module layout is presented in figure 3b, where two half-bridge modules and one common source device are implemented. It is estimated that the switching loss, and therefore thermal energy loss, given by the common source is 30% greater than a single half-bridge module. The volume of the inverter minus the cold plate is 4.6 L with a mass of 3.4 kg. For control purposes, a 6-pass copper tube, aluminum body off-the-shelf liquid cold plate was used as a baseline comparison. Mounting hardware attached the power modules at each corner for a total of 12 screws, with each being tightened to a torque of 3 nm. This ensured sufficient contact pressure for the interfacial thermal interface layer across all three modules. Wakefield-Vette 126-4 thermal paste was used as the interface layer with a thermal conductivity of 0.69 W/m-K. A sponge roller was used to apply a uniform paste layer across the entire contact area between the modules and cold plate.

5.4.2 IMPINGEMENT COOLER INTEGRATION

Figure 4a presents the assembled single-phase inverter with integrated non-metallic jet impingement coolers. Each cooler has separate inlet and outlet ports that are independent of other devices. As opposed to printing a single cooler with jet locations aligning with module hot spots, this method enabled the flow rate to each device to be controlled for the purpose of thermally balancing the system. Using the same mounting points as the cold plate, sufficient torque is applied to the mounting bolts to ensure a completely sealed interface between the cooler and power module. Additionally, these bolts are uniformly tightened as to avoid warping the module base plate and damaging the internal components. As seen in Figure 1b, the default configuration of the cooler has the inlet and outlet paths in-line with each other. This is not compatible with the T-type

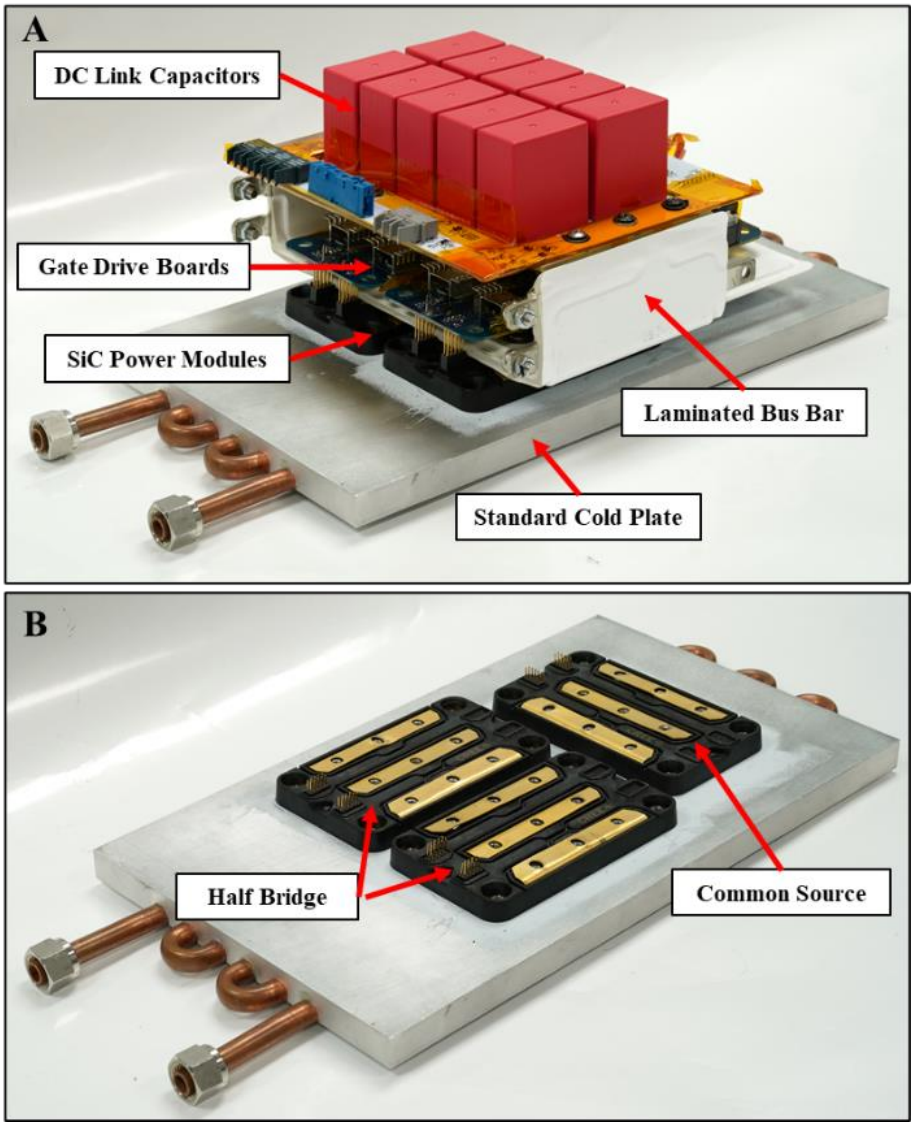

Figure 3: A) 150 kW inverter overview with component callouts. B) T-type module arrangement including two half-bride modules and one common source.

arrangement; therefore, the coolers attached to the half-bridge modules required a 90-degree outlet turn. Figure 4b shows this modification, and additionally calls out the location of the interfacial gasket material. The standoffs seen below each cooler are present to provide spacing for coolant routing connections.

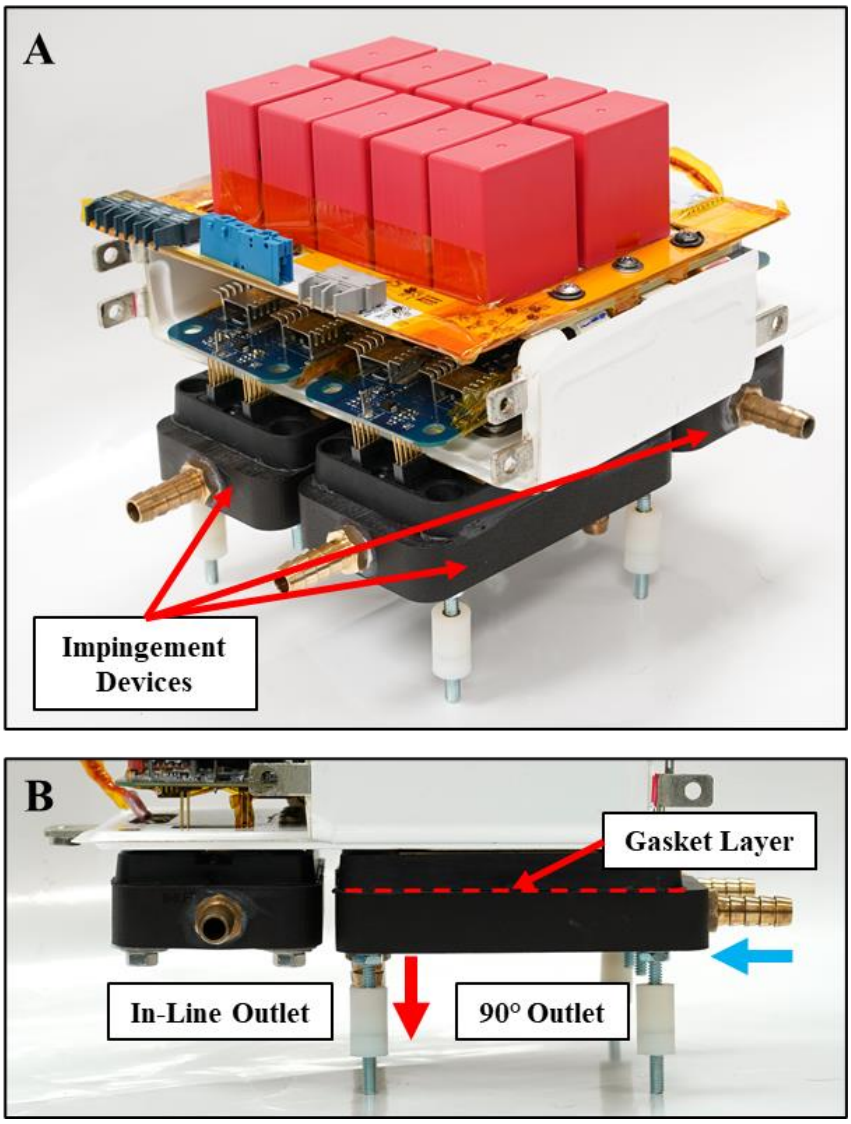

Figure 4: A) Inverter assembly with integrated impingement coolers. B) Description of outlet path modifications and gasket material locations.

5.5 ELECTROMAGNETIC INTERFERENCE IMPROVEMENTS

5.5.1 EMI EVALUATION SETUP

In previous studies it was shown that the non-metallic jet impingement cooler can provide a reduction in EMI noise by de-coupling the power module from a common ground [19-20]. Double-pulse tests were performed on a single power module at relatively low voltage levels on the order of 100 V. To test the scalability of the non-metallic material benefits, it was determined

a continuous test at high voltage was needed to examine the EMI noise and common mode current over-shoot present in the multi-module arrangement. Figure 5 presents the test setup to evaluate the EMI reduction capability of the non-metallic impingement cooler. Compared to a standard double-pulse test, this setup required the addition of networks to stabilize the line impedance of the system. As a benchmark, the standard cold plate is directly placed onto the copper ground plane, as would typically be done in power electronics systems to avoid energizing the internal coolant. With the impingement cooler setup, the devices were also placed directly onto the copper plane, but with no metallic fasteners contacting the copper. Continuous tests at up to 500 V were performed, more than five times the level previously demonstrated.

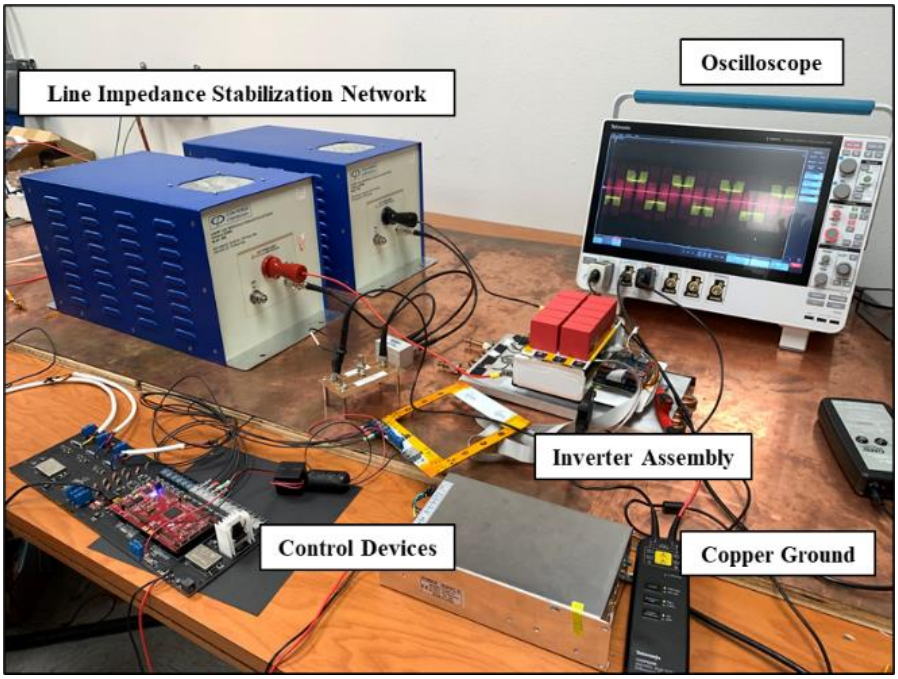

Figure 5: EMI noise evaluation setup configured for 500 V continuous testing.

5.5.2 HIGH VOLTAGE COMMON MODE NOISE RESPONSE

Figure 6 presents a spectrum comparison of common mode noise between the standard cold plate and additively manufactured heat sink (AMHS). In the frequency range below 10 MHz, a consistent 26 dB reduction of noise is observed. Above this threshold, the noise reduction varies

between 5 and 25 dB of improvement. This result is consistent with previously shown benefits. However, the main difference being the parasitic capacitance pathways contributing towards EMI accentuation are consistently reduced using the non-metallic coolers on the system-level scale.

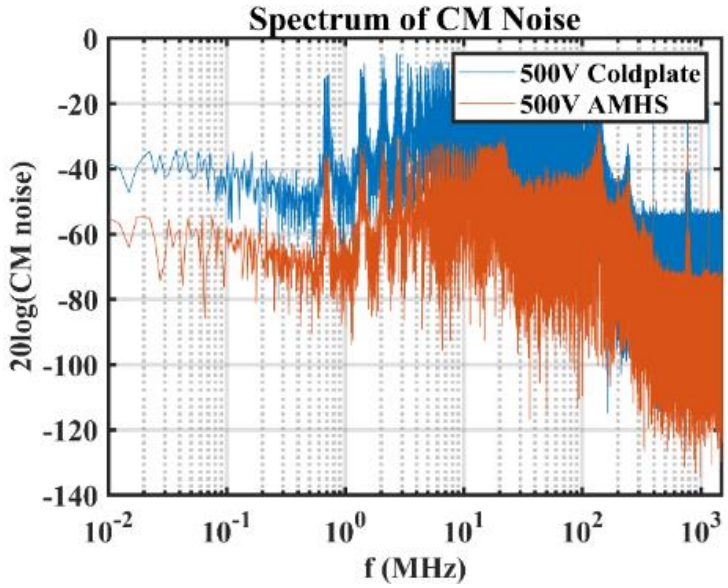

Figure 6: Common mode noise response of the single-phase inverter.

In addition to assessing the EMI noise, the common mode current overshoot was also observed. Figure 7 shows the common mode current waveform at progressively decreasing time intervals measured at the same point in the collected data stream. The bottom-most image of each cooling type displays the maximum current overshoot, with the non-metallic cooler reducing this value from 110 A in the cold plate system down to 11 A. In previous low voltage evaluations, a reduction of 61% was observed. At the 500 V level with three parallel modules, a 90% reduction is measured. From these results, it can be concluded that not only does the cold plate accentuate the EMI noise at a greater level in the single-phase inverter setup, but also that the impingement cooler drastically dampens current ringing.

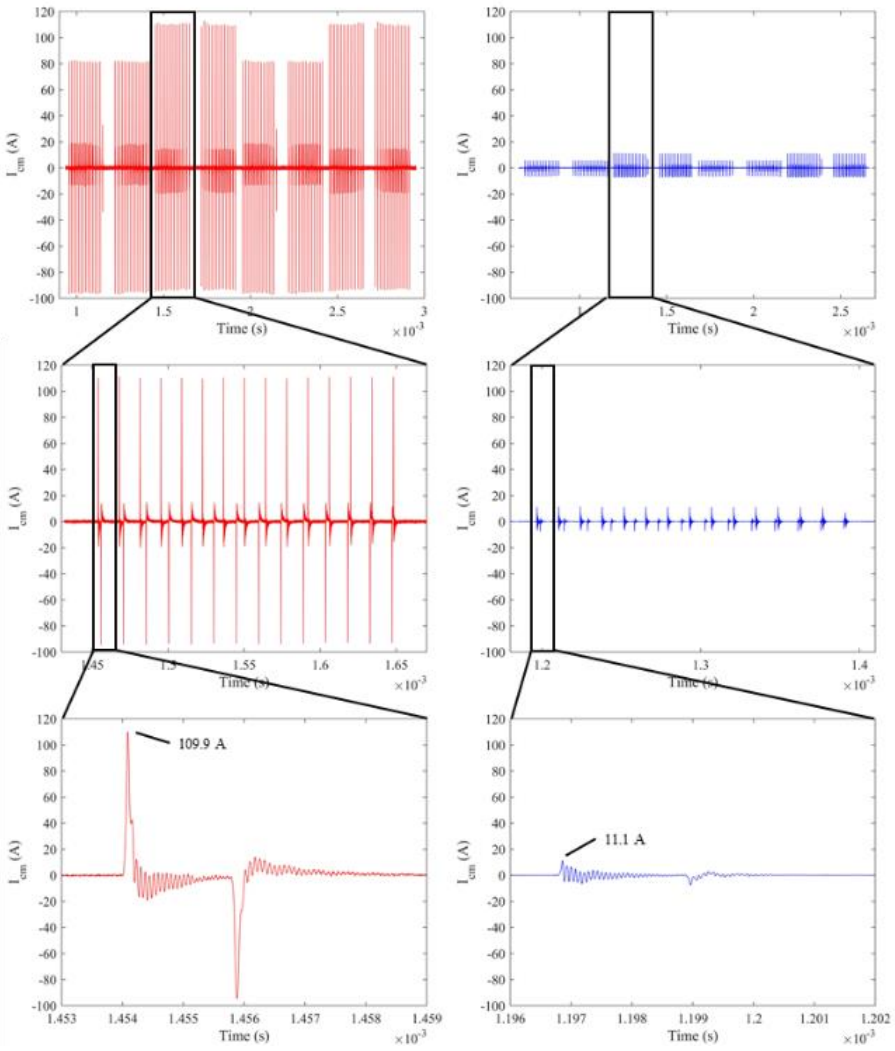

Figure 7: Comparison of common mode current overshoot with the cold plate (left) and impingement cooler (right).

5.6 HIGH VOLTAGE INVERTER THERMAL MANAGEMENT

To evaluate the thermal management capabilities of the three impingement devices and cold plate, the experimental testing configuration see in figure 8 was constructed. Using a DC power supply with an inductive load, the single-phase inverter was analyzed at four amperage levels: 100, 150, 175 and 200 A. RTDs located inside the power modules provided an estimated average junction temperature. An IR camera capture the case temperatures on the half bridge 1 module to evaluate the thermal gradients and maximum temperature differences. The coolant loop

included a centrifugal pump operating at maximum load, giving a flow rate between 1.85-1.95 gpm depending on the pressure drop of the cooling system. Water at 25 °C was the cooling medium and was held constant by an external chiller apparatus. Finally, manifold blocks and control values were used to control the flow rate to each impingement device to provide thermal balancing if required.

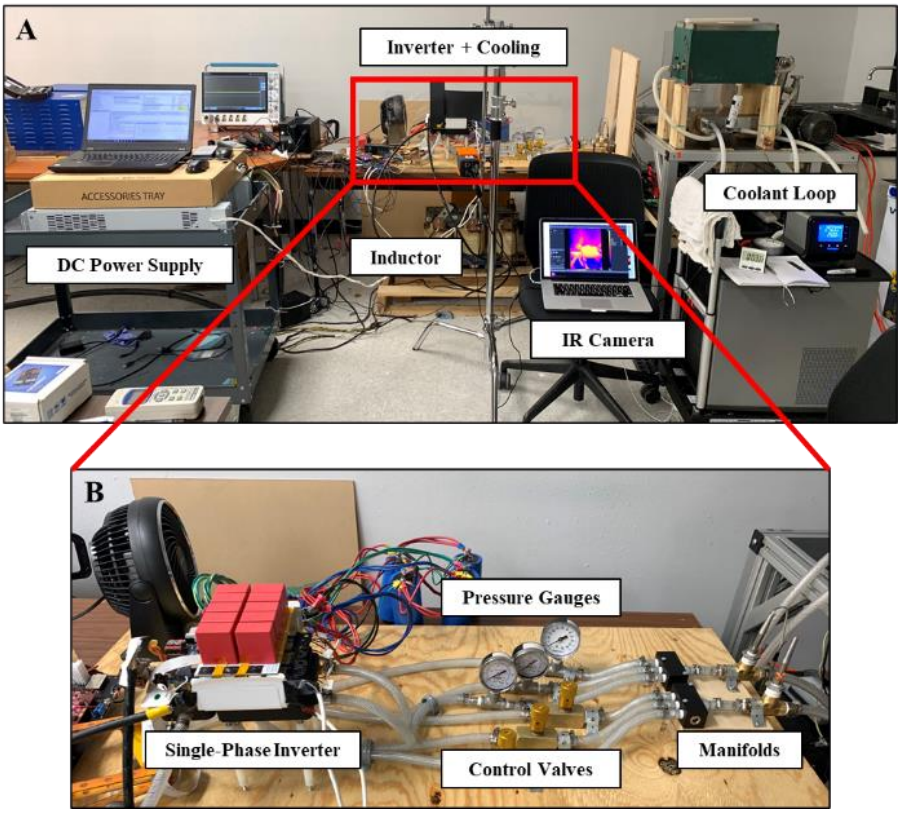

Figure 8: A) Experimental setup overview with electrical and thermal callouts. B) Close-up view of the test section with coolant routing lines.

5.6.1 THERMAL TESTING COOLANT CONFIGURATIONS

To achieve thermal balancing between power modules with varying operating power levels, it was critical to provide adaptable cooling arrangements when achievable. The baseline configuration with the cold plate, figure 9, required only one inlet and outlet path as all three modules were attached to the aluminum block. Regarding the layout of the modules on the cold

plate, the two half bridge devices were placed closer to the plumbing connections as this is where much of the power load is centered. Thus, it is advantageous to locate these devices closer to the coldest side of the cold plate to limit co-heating effects.

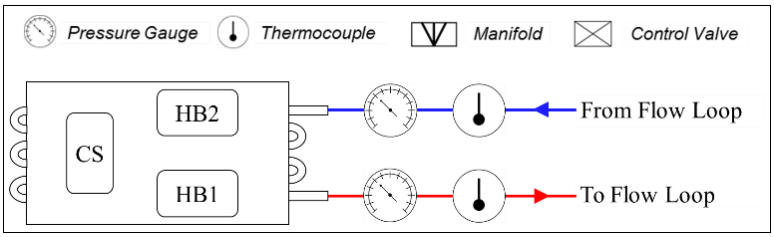

Figure 9: Control cooling arrangement using the standard cold plate with single inlet and outlet paths.

For this study, three separate impingement devices are attached to individual modules. With each cooler having inlet and outlet ports, there are multiple options with respect to coolant routings. Figure 10 presents diagrams of three distinct coolant configurations. First, the “Parallel” method, figure 10a, splits the incoming coolant equally across the three coolers. Since the same cooler design is used for each module, the pressure drop is evenly divided. Given that the common source module generates higher switching losses, it can be reasonably assumed a large temperature discrepancy will be present in this base configuration. Therefore, a flow control valve is placed in series with each cooler. By re-routing more mass flow to the common source module, this device will experience a lower internal temperature, leading to a reduced thermal inconsistency between modules.

The second configuration shown in figure 8b chains the modules in series. Each cooler passes the maximum flow rate, beginning with the highest power module and followed by the two half bridges. Compared to the parallel method, the series layout will inherently create larger pressure drops as the flow rate through each device is tripled, while in conjunction reducing internal module temperatures.

The last layout, figure 8c, flows the maximum flow rate through the common source cooler and then divides in half for each half bridge. It is hypothesized this configuration will achieve a similar result to the parallel case with balancing valves, but without the added hardware.

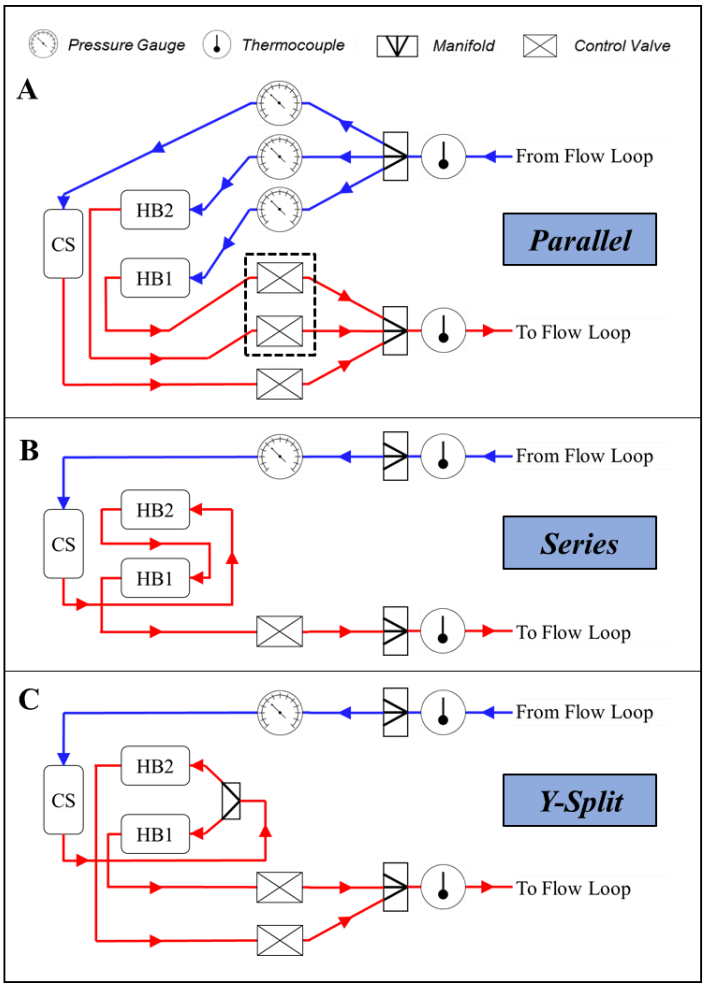

Figure 8: Coolant routing configurations for the impingement coolers including A) parallel, B) series, and C) y-split arrangements.

5.6.2 THERMAL MANAGEMENT RESULTS

Figure 9 presents the internal RTD temperature response of each power module at the 200 A operation as this was the only level the control valves were implemented due to testing constraints. Also shown in the figure are the maximum temperature difference for each cooling arrangement and the corresponding average module temperature. As expected, the cold plate

produces a large temperature variation of 6°C between the common source and half bridge modules due to its inability to allocate cooling where needed. Comparatively, the unbalanced parallel setting drops this temperature difference down to 4.9 °C and reduces the average temperature by 0.5 °C. When the half-bridge control values are initiated, the temperature difference jumps down to 1.8 °C due to the common source and half bridge modules experiencing a decrease and increase in temperature, respectively. Finally, the series and y-split arrangements maintain this reduced temperature difference while simultaneously lowering the average temperature by another 0.5 °C.

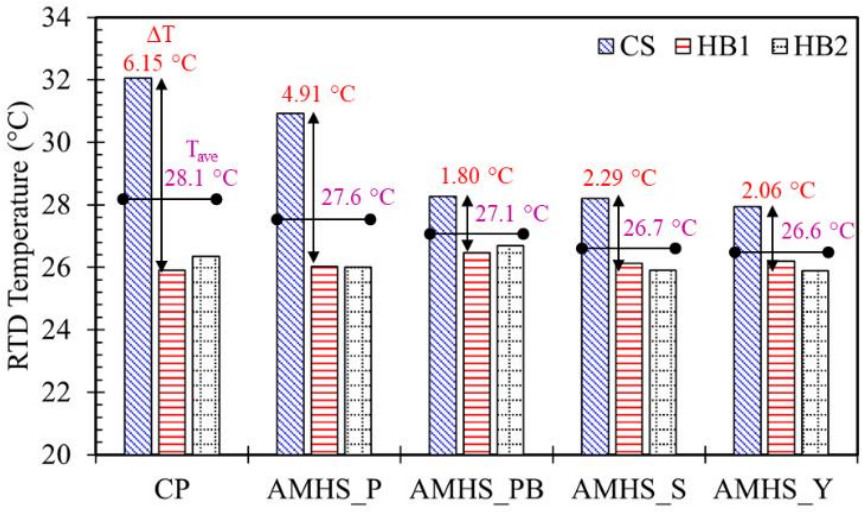

Figure 9: Internal power module RTD temperature readouts for the 200 A inverter operation setting.

During testing, the total pressure drop across each hydraulic circuit was measured. Using equation 1, this pressure was converted into an effective pumping power where V is the volumetric flow rate.

$$P_{pump} = \dot{V} * \Delta P \quad (1)$$

Using pumping power as a performance metric enables the comparison of added system requirements for each coolant circuit. Figure 10 presents the thermal imbalance between modules

plotted against the corresponding pumping power. It is clear there is a definite relationship between thermal performance and pumping cost. The default parallel impingement setup presents the lowest pumping costs by virtue of only 1/3rd the total flow rate passing through each cooler. The jet impingement performance is therefore limited by the reduced jet Reynolds numbers. On the contrary, the balanced parallel, y-split and series show excellent thermal balancing, but come at a steep pumping cost. As expected, the series arrangement requires the greatest upstream pressure given each impingement cooler has 100% of the flow rate passing through. When comparing the parallel balanced and y-split setups, the hypothesis that thermal balancing can be achieved simply through coolant routing without control valves is upheld. During testing, the control valves were restricted to the greatest extent as to also maintain a safe cooling threshold to avoid thermal runaway. Inherently the flow rate redirected to the common source module could never reach its full value as that would cut-off cooling to the rest of the system. This explains why the pressure drop was slightly greater in the y-split circuit as the maximum flow rate passed through the common source cooler. However, it is reasonable to say that these two hydraulic circuits present approximately equivalent thermal imbalance and pumping power requirements, but with the y-split system presenting a more reasonable approach by eliminating pumping system complexity.

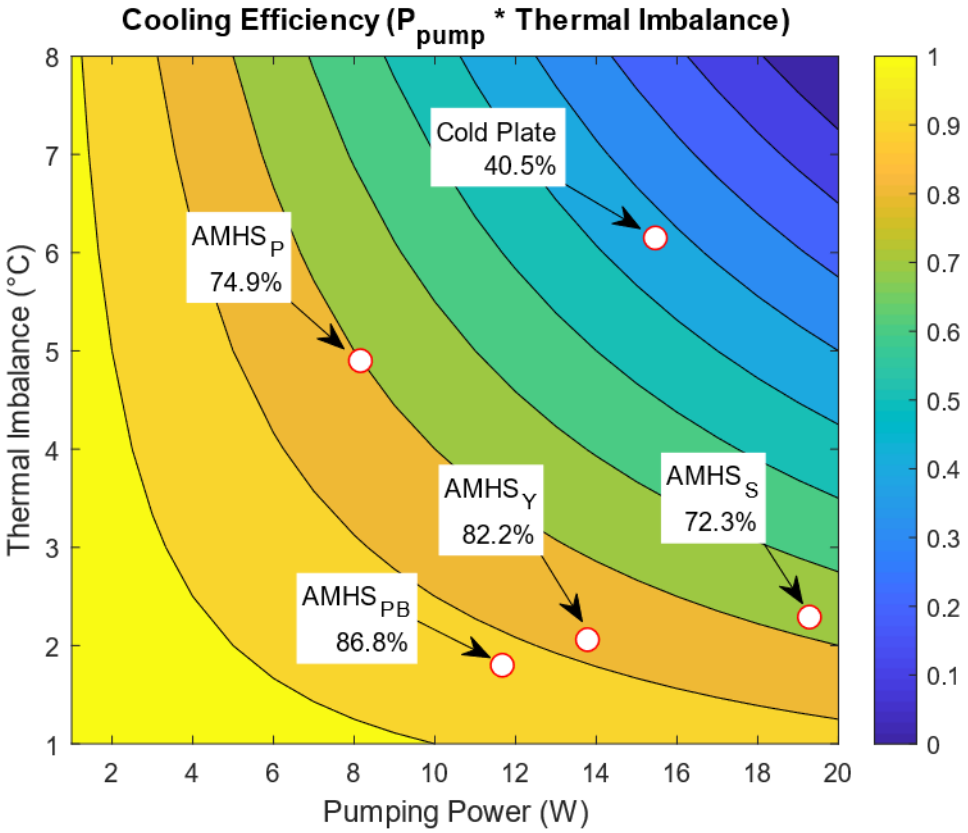

Figure 10: Cooling efficiency of each thermal management arrangement with respect to thermal imbalance and pumping power.

As shown in figure 8, an IR camera was used to measure the case temperature of the half-bridge 1 module. This exercise served two purposes: monitoring critical inverter points for overheating and to capture the temperature gradients along the HB1 module. Figure 11 presents the temperature data capture by the camera for each current setting. The direct cooling of the module hot spots contributes to the reduction in temperature variation seen in figure 11a. Compared to the cold plate, the impingement coolers reduce the temperature differences by 1°C, with the greatest effect seen at the higher amperage levels. This improvement does not directly carry over to the average case temperature, however. Given that the cold plate is in contact with more surface of the module base, one might expect the local hot spots to be greater, but overall have a lower average temperature. Figure 11b shows just this as there is little improvement using

the impingement coolers over the cold plate with respect to average case temperatures. Combined, Figures 11a and 11b demonstrate how the impingement cooler advantages mainly lie in the reduction of local hot spots, while enabling cross-module thermal balancing.

To summarize the effect of each cooling configuration on various systematic metrics, a spider chart is presented in figure 12. Four metrics are normalized where 0 is the worst performing and 1 is the best performing. The maximum module

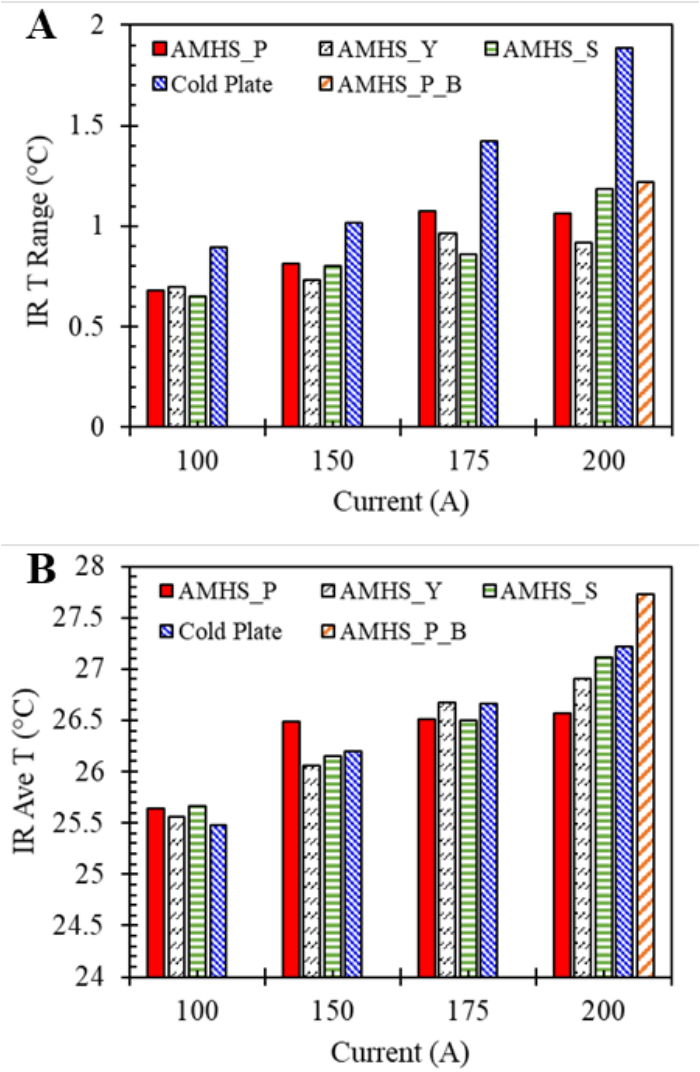

Figure 11: A) Maximum case temperature difference in module HB1 captured by IR imaging. B) Average case temperatures with respect to each cooling method and parametric amperage settings.

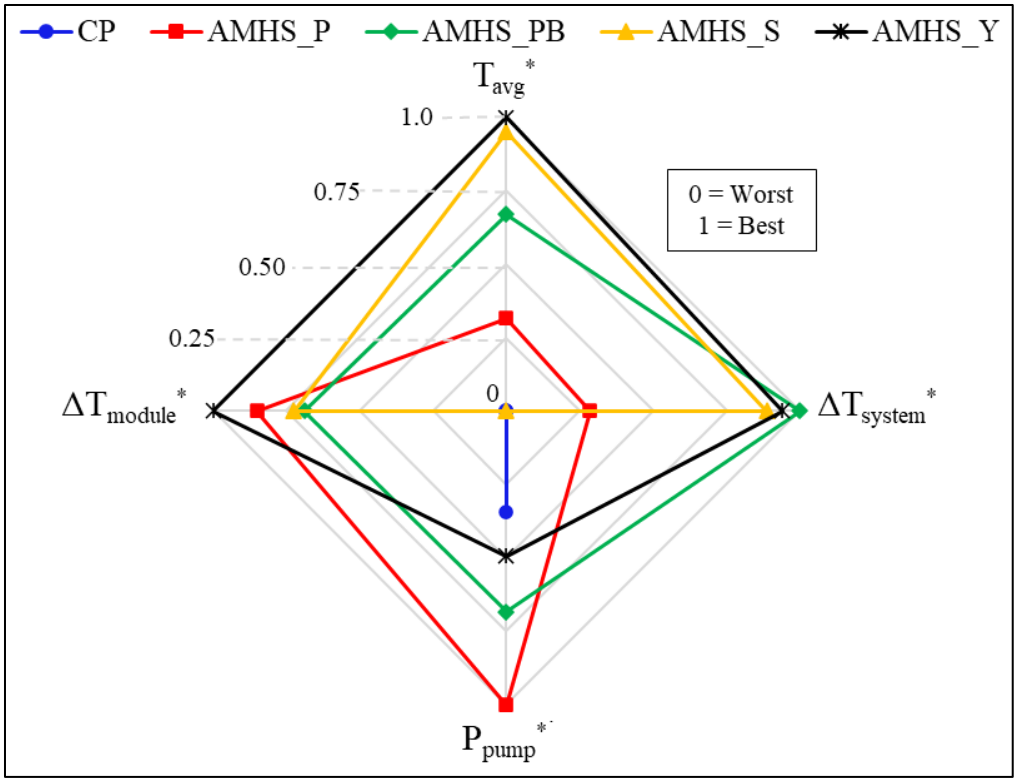

Figure 12: Normalized performance metrics summarizing the benefits and drawbacks of each cooling arrangement.

case temperature difference, average module RTD temperature, maximum thermal imbalance and pumping power values are included. It is clear to see that the standard cold plate performs the worst in all categories except for pressure drop where only the AMHS_S setup required more pumping power. In general, the most appropriate cooling configuration is highly dependent on the systematic constraints. If pumping power is not a concern but average module temperatures need to be minimized, the impingement cooler series and y-split setups are best. If pumping power is highly constrained but module temperatures can be slightly higher, then the parallel impingement cooler arrangement might be the correct method. Finally, if cross-module thermal imbalance is a critical metric, then the balanced parallel condition using control values could be employed.

5.7 COMPARISION TO POWER ELECTRONICS GOALS

It is well accepted for hybrid-electric propulsion systems, the power electronics must achieve a specific power greater than 20 kW/kg [23]. This is largely driven by the fact that many other components of electrified transportation such as batteries and motors are still in their infant stages of integration. Thus, a maximized specific power from the power electronics components will ensure downstream equipment can be optimized. Motivated by the need to improve transportation emissions and reduce the dependence on non-renewable resources, various companies and groups have proposed specific power targets that should be met to ensure successful transition to electric transport. Table 1 presents a summary of specific power targets, with a deadline on or before the year 2025. Additionally, the resulting specific power achieved with the impingement coolers is presented. Compared to the standard cold plate, the non-metallic coolers increase the specific power by 40%.

TABLE 1

Source	Year	Specific Power (kW/kg)
NASA [24]	2025	25
GE [25]	2020	19
APCUK [26]	2025	20
ORNL [27]	2020	14
PSMA [28]	2020	19
NAP [29]	2025	15
This work	2021	38

5.8 CONCLUSIONS

This work has proposed the integration of non-metallic jet impingement coolers with a high-voltage hybrid electric propulsion inverter for improved thermal and electrical performance. Substituting a standard metallic cold plate with nylon-based thermal management reduced EMI noise by 26 dB and common mode current overshoot by 90%. With respect to the thermal management performance, utilizing one impingement cooler per power module enabled systematic thermal balancing that is otherwise unachievable with traditional cooling techniques. Thermal imbalances created by non-uniform module switching losses were reduced using a combination of custom coolant routing and control valves. Furthermore, it was shown that thermal balancing can be achieved by leveraging hydraulic circuit networks that focus the coolant into critical areas while simultaneously keeping pressure drop at a reasonable level.

In terms of the overall effectiveness of the non-metallic jet impingement cooler, it has been shown to create uniform internal device temperatures while maintaining the integration flexibility to be effective on the systematic scale. Achieved largely through additive manufacturing techniques, this research area has the potential to be a very important part of achieving industry power electronics goals for the purpose of reducing the carbon footprint of energy and transportation sectors.

5.9 ACKNOWLEDGMENTS

This work was supported by the National Science Foundation Engineering Research Center for Power Optimization of Electro-Thermal systems (POETS) with cooperative agreements EEC-1449548. Any opinions, finding, and conclusions or recommendations expressed in this material are those of the author(s) and do not necessarily reflect the views of the National Science Foundation.

5.10 REFERENCES

[1] F. Zare, D. Kumar, M. Lungeanu, and A. Andreas, "Electromagnetic interference issues of power, electronics systems with wide band gap, semiconductor devices," 2015, no. Conference Proceedings, pp. 5946-5951, doi: 10.1109/ECCE.2015.7310494.

[2] H. Lu, C. Bailey, and C. Yin, "Design for reliability of power electronics modules," Microelectronics Reliability, vol. 49, no. 9, pp. 1250-1255, 2009/09/01/ 2009, doi: https://doi.org/10.1016/j.microrel.2009.07.055.

[3] C. Durand, M. Klingler, D. Coutellier, and H. Naceur, "Power Cycling Reliability of Power Module: A Survey," *IEEE Transactions on Device and Materials Reliability*, vol. 16, no. 1, pp. 80-97, 2016, doi: 10.1109/TDMR.2016.2516044.

[4] P. McCluskey, "Reliability of Power Electronics Under Thermal Loading," 2012, no. Conference Proceedings, pp. 1-8.

[5] R. W. Johnson, C. Wang, Y. Liu, and J. D. Scofield, "Power Device Packaging Technologies for Extreme Environments," *IEEE Transactions on Electronics Packaging Manufacturing*, vol. 30, no. 3, pp. 182-193, 2007, doi: 10.1109/TEPM.2007.899158.

[6] M. J. Palmer, R. W. Johnson, T. Autry, R. Aguirre, V. Lee, and J. D. Scofield, "Silicon Carbide Power Modules for High-Temperature Applications," *IEEE Transactions on Components, Packaging and Manufacturing Technology*, vol. 2, no. 2, pp. 208-216, 2012, doi: 10.1109/TCPMT.2011.2171343.

[7] R. Khazaka, L. Mendizabal, D. Henry, and R. Hanna, "Survey of High-Temperature Reliability of Power Electronics Packaging Components," *IEEE Transactions on Power Electronics*, vol. 30, no. 5, pp. 2456-2464, 2015, doi: 10.1109/TPEL.2014.2357836.

[8] G. Moreno, S. Narumanchi, X. Feng, P. Anschel, S. Myers, and P. Keller, "Electric-Drive Vehicle Power Electronics Thermal Management: Current Status, Challenges, and Future Directions," *Journal of Electronic Packaging*, vol. 144, no. 1, 2021, doi: 10.1115/1.4049815.

[9] M. Reeves, J. Moreno, P. Beucher, S.-J. Loong, and D. Bono, "Pushing the limits of liquid cooling: Design and analysis of a direct liquid cooling system for power modules," International Journal of Microscale and Nanoscale Thermal and Fluid Transport Phenomena, vol. 4, no. 1, p. 71, 2013.

[10] T. Acikalin and C. Schroeder, "Direct liquid cooling of bare die packages using a microchannel cold plate," 2014, no. Conference Proceedings, pp. 673-679, doi: 10.1109/ITHERM.2014.6892346.

[11] C. Qian et al., "Thermal Management on IGBT Power Electronic Devices and Modules," IEEE Access, vol. 6, pp. 12868-12884, 2018, doi: 10.1109/ACCESS.2018.2793300.

[12] J. Kim, "Spray cooling heat transfer: The state of the art," International Journal of Heat and Fluid Flow, vol. 28, no. 4, pp. 753-767, 2007/08/01/ 2007, doi: https://doi.org/10.1016/j.ijheatfluidflow.2006.09.003.

[13] P. R. Parida, S. V. Ekkad, and K. Ngo, "Impingement-based high performance cooling configurations for automotive power converters," International Journal of Heat and Mass Transfer, vol. 55, no. 4, pp. 834-847,2012/01/31/2012,doi:https://doi.org/10.1016/j.ijheatmasstransfer.2011.10.024.

[14] M.-S. Shin, S. Senguttuvan, and S.-M. Kim, "Investigations of Flow and Heat Transfer Characteristics in a Channel Impingement Cooling Configuration with a Single Row of Water Jets," Energies, vol. 14, no. 14, p. 4327, 2021.

[15] L. Lin and R. Ponnappan, "Heat transfer characteristics of spray cooling in a closed loop," International Journal of Heat and Mass Transfer, vol. 46, no. 20, pp. 3737-3746, 2003/09/01/ 2003, doi: https://doi.org/10.1016/S0017-9310(03)00217-5.

[16] K. Gould, S. Q. Cai, C. Neft, and A. Bhunia, "Liquid Jet Impingement Cooling of a Silicon Carbide Power Conversion Module for Vehicle Applications," IEEE Transactions on Power Electronics, vol. 30, no. 6, pp. 2975-2984, 2015, doi: 10.1109/TPEL.2014.2331562.

[17] B. Mouawad, R. Skuriat, J. Li, C. M. Johnson, and C. DiMarino, "Development of a highly integrated 10 kV SiC MOSFET power module with a direct jet impingement cooling system," in 2018 IEEE 30th International Symposium on Power Semiconductor Devices and ICs (ISPSD), 13-17 May 2018 2018, pp. 256-259, doi: 10.1109/ISPSD.2018.8393651.

[18] A. Bhunia and C.-L. Chen, "Jet Impingement Cooling of an Inverter Module in the Harsh Environment of a Hybrid Vehicle," presented at the ASME 2005 Summer Heat Transfer Conference collocated with the ASME 2005 Pacific Rim Technical Conference and Exhibition on Integration and Packaging of MEMS, NEMS, and Electronic Systems, 2005. [Online]. Available: https://doi.org/10.1115/HT2005-72574.

[19] R. Whitt, D. Huitink, A. Emon, A. Deshpande, and F. Luo, "Thermal and Electrical Performance in High-Voltage Power Modules With Nonmetallic Additively Manufactured Impingement Coolers," IEEE Transactions on Power Electronics, vol. 36, no. 3, pp. 3192-3199, 2021, doi: 10.1109/TPEL.2020.3015226.

[20] R. Whitt, S. J. Hudson, D. Huitink, Z. Yuan, A. Emon, and F. Luo, "Additive Manufactured Impinging Coolant, Low EMI, & Non-Metallic Heat Spreader: Design and Optimization," Journal of Electronic Packaging.

[21] N. Zuckerman and N. Lior, "Jet Impingement Heat Transfer: Physics, Correlations, and Numerical Modeling," vol. 39, G. A. Greene, J. P. Hartnett†, A. Bar-Cohen, and Y. I. Cho, Eds., ed: Elsevier, 2006, pp. 565-631.

[22] Z. Yuan et al., "A Three-phase 450 kVA SiC-MOSFET Based Inverter With High Efficiency and High Power Density By Using 3L-TNPC," in 2021 IEEE Applied Power Electronics Conference and Exposition (APEC), 14-17 June 2021 2021, pp. 2171-2176, doi: 10.1109/APEC42165.2021.9487253.

[23] A. Deshpande, Y. Chen, B. Narayanasamy, Z. Yuan, and F. Luo, "Modular Three-level T-type Power Electronics Building Block for Aircraft Electric-Propulsion Drives," in 2020 AIAA/IEEE Electric Aircraft Technologies Symposium (EATS), 26-28 Aug. 2020 2020, pp. 1-8.

[24] J. Felder, “NASA Electric Propulsion System Studies,” EneryTech 2015, 2016.

[25] R. Jansen et al., “Overview of NASA Electrified Aircraft Propulsion Research for Large Subsonic Transports,” EnergyTech 2017, 2017.

[26] Advanced Propulsion Centre UK, “Power Electronics Roadmap 2020,” 2021.

[27] O. Burak et al., “Electric Drive Technologies Roadmap Update,” Oak Ridge National Laboratory, 2017.

[28] T. O’Connell, “Aircraft Power Electronics: Trends, Obstacles and Opportunities,” PSMA, 2017.

[29] B. Sarlioglu, “Electrification of Aircraft and Vehicles: Current Status and Future Trends,” WEMPEC, 2018.

6. CONCLUSION

6.1 SUMMARY OF RESULTS

The research presented in this manuscript describes the design, manufacturing, testing and integration of a non-metallic jet impingement cooler for high-voltage power electronics devices. The performance and efficacy of the cooler was evaluated using simulated and experimental techniques to examine the local and systematic benefits with respect to thermal and electrical efficiency.

Additive manufacturing techniques were employed to fabricate the complex internal fluid pathways in a watertight, lightweight, nonmetallic framework. The materials were shown to withstand the high-pressure operating conditions, with specific post processing methods improving surface roughness using chemical vapor smoothing, thereby reducing overall pumping requirements.

Using electromagnetic interference tests, a drastic reduction in common mode noise throughout a power electronics system was observed when a standard cold plate was replaced with the non-metallic impingement cooler. Parasitic capacitance pathways were reduced by 99%, directly leading to a 25 dB drop in noise. With respect to EMI, dampening this electronic ringing effect with a non-metallic cooler can enable the use of smaller shielding components, improving power density and specific power ratings.

Computational fluid dynamics conjugate heat transfer simulations were used to first evaluate the cooling performance. A three-module setup was replicated with critical hot spots being targeted by individual jets. From this analysis, it was found that not only did the jet impingement method reduce average temperatures, but temperature uniformity among die locations was achieved.

To experimentally validate these results, a hot-spot emulating heating block was constructed to mimic high-voltage power module switching losses. Results show that thermal gradients were effectively eliminated compared to a standard cold plate, while also reducing maximum temperatures by 40 °C. Moreover, the results of the heating block can be directly compared to the predicted cooling performance based off of empirical correlations. Using equation 1 in Chapter 2, the average Nusselt number can be estimated. Table 1 below gives the experimental parameters that are necessary for the comparison. The average experimental local heat transfer coefficient between the 14 die locations was approximately 100 kW/m2-K and an average Nusselt number of 258. Using the single round jet empirical correlation with an impingement area equal to that of the heating block hot spots, the predicted average Nusselt number is 252, giving a percent error of 2.3%. These values are very closely aligned, meaning that using jet impingement correlations is an effective method of estimating thermal management performance before computational and experimental studies are initiated.

TABLE 1

Parameter	Value
Height, H	5 mm
Diameter, D	1.5mm
Pr	7
Re	7632
Heater Assembly Thermal Resistance	1.18 K/W
Distance from impingement point, r	3 mm

Finally, full-scale integrated testing was performed with a 150-kW hybrid-electric propulsion inverter. As opposed to the device-scale analysis given by the heating block, this

experiment showed the efficacy of using multiple impingement devices for systematic thermal balancing. Various coolant routing arrangements were demonstrated, with each one achieving lower thermal imbalance between power modules than the cold plate. Furthermore, it was demonstrated how each specific cooling configuration can achieve similar results with different equipment requirements and overall pressure drop.

6.2 CONCLUSIONS AND FUTURE OUTLOOK

Additive manufacturing has enabled high performance thermal management to be directly integrated with power electronics systems. The non-metallic materials used immediately improve power density and specific power ratings, which aid in meeting industry targets by 2025. Jet impingement cooling, while lower performing than some two-phase methods, is easily achieved with additive techniques and can be quickly customized for a specific electrical layout. Therefore, it is easy to see why in addition to weight and EMI benefits, non-metallic 3D printing should be highly integrated in a thermal management design space.

While the static jet impingement device effectively cooled critical hot spots, the cooler must be designed for the highest power rating of the electrical system. At low power operations, this may result in wasted pumping power and unnecessary hydraulic stresses on the cooler. An active jet impingement cooler with varying geometry nozzles would allow feedback loops between power module temperatures and pumping power to optimize the cooling as needed. Additionally, if a specific area of a power module were to start failing, thus producing more switching losses, the active jet scheme could route more cooling to this section to prevent failure until maintenance can occur. And finally, the active jet would have the potential to further enhance local heat transfer through pulsating flows. In conjunction with the ability to reallocate cooling resources, the variable

geometry jet impingement cooler might be the next step to advance the thermal management of power electronics.